

DERIVING WATER QUALITY INDICATORS OF LAKE TANA, ETHIOPIA, FROM LANDSAT-8

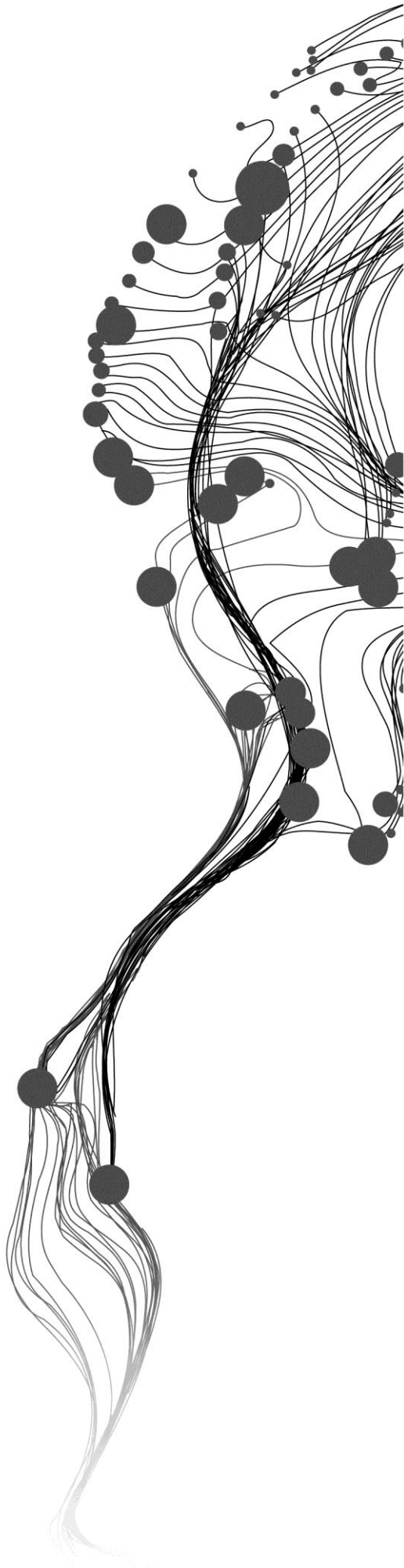
TESHALE TADESSE DANBARA

February, 2014

SUPERVISORS:

Dr. ir. Mhd. (Suhyb) Salama

Dr. ing. T.H. Rientjes



DERIVING WATER QUALITY INDICATORS OF LAKE TANA, ETHIOPIA, FROM LANDSAT-8

TESHALE TADESSE DANBARA

Enschede, The Netherlands, February, 2014

Thesis submitted to the Faculty of Geo-Information Science and Earth Observation of the University of Twente in partial fulfilment of the requirements for the degree of Master of Science in Geo-information Science and Earth Observation.

Specialization: Water Resources and Environmental Management

SUPERVISORS:

Dr.ir.Mhd.(Suhyb) Salama

Dr.ing.T.H. Rientjes

THESIS ASSESSMENT BOARD:

Prof. Dr. Ing. W. Verhoef (Chair)

Dr. M.R. Wernand (External Examiner, Royal Netherlands Institute for Sea Research, Texel)

DISCLAIMER

This document describes work undertaken as part of a programme of study at the Faculty of Geo-Information Science and Earth Observation of the University of Twente. All views and opinions expressed therein remain the sole responsibility of the author, and do not necessarily represent those of the Faculty.

I would like to dedicate this thesis to my precious and beloved wife Mulu Bogale, for all of her love, support, encouragement and patience.

ABSTRACT

The purpose of this study is to derive the water quality indicators of the Lake Tana from the recently launched satellite Landsat-8 using in-situ measurement and hydro-optical inversion model Hydrosat. In-situ water quality variables and radiometric measurements were carried out in September 2013 which is at the end of rainy season. The downwelling irradiance and upwelling radiance measured in the field and concentration of suspended particulate matter (SPM), coloured dissolved organic matter (CDOM), Chlorophyll-a absorption and turbidity from lake water samples were measured in the laboratory. The field measured Ramses spectral data was analysed and the Landsat-8 relative spectral response (RSR) has been simulated by interpolated Ramses data. The spectral ranges of Ramses data to work accompany with the first five operational land imager (OLI) bands of Landsat-8 and the central wavelengths of Landsat-8 to retrieve the water quality variables were determined. The Hydrosat inversion model is selected for this study. The model derives all relevant water quality variables. For this study the model has been modified to retrieve the water quality indicators of Lake Tana from Landsat-8. Also an atmospheric correction scheme for Landsat-8 has been developed. Results of this study on applicability of Landsat-8 for retrieval of water quality indicators are promising. Compared to its predecessor newly added bands of Landsat-8 such as band-1 and band-9 have been found useful for the retrieval of the water quality indicators. The field data has been used to calibrate and to validate the derived IOPs using calibration and validation of geophysical observation model (GeoCalVal). The specific inherent optical property (SIOP) of SPM of Lake Tana has been estimated. The derived backscattering coefficient of suspended particulate matter (SPM) and the absorption coefficient of detritus and gelbstoff with the measured concentration of SPM have shown linear relationships with R-squared value of greater 0.7. The time-space distribution of the water quality indicators of Lake Tana has been investigated for four seasons. The absorption of detritus and gelbstoff is high along the lake shore and the backscattering coefficient of SPM is low across the lake in dry season. In peak rainy season the IOPs are distributed within the same pattern across the lake and their higher values are observed along the lake shore and in the rivers outlet area. At the end of rainy season the absorption coefficient of detritus and gelbstoff is high across the lake and the backscattering coefficient of SPM is high in the west part of the lake. Furthermore, the IOPs are distributed across the lake with the higher value in the northern part shortly after the end of rainy season. The study has shown that the most dominant water quality variable which predominantly affects the IOPs of Lake Tana is SPM. The main source of SPM in Lake Tana is the sediment load from the tributaries and from the erosion of the agricultural land around the lake during rainy season.

Key Words: Lake Tana, Landsat-8, Water quality indicators, Hydro-optics

ACKNOWLEDGEMENTS

First and foremost, I must acknowledge and thank the almighty God for His provision, protection, guidance and comfort throughout my life. I could never have accomplished this without the mercy, grace and help of the heavenly father.

I would like to express my special appreciation and thanks to my first supervisor Dr.ir.Mhd.(Suhyb) Salama for his useful guidance, comments, motivation and encouragement throughout the thesis work. It's really privilege to work with him and his in-depth knowledge of the remote sensing of water quality has been appreciated. Furthermore I would like to thank my second supervisor Dr.ing.T.H.Rientjes for supporting and guiding me to arrange my field work and for the critical comments he made on the thesis.

I would like to thank Dr. Essayas Kaba for being very good friend and advisor. I have found him the one who has always been caring and ready to help me.

I would like to thank the Royal Netherlands Government for funding this study through the Netherlands fellowship program. I will never and ever forget the input and knowledge I have gotten from the staff members of water resources and environmental management department at ITC university of Twente. You all have put a finger print and it's sincerely appreciated. Also I would like to thank Bahir Dar University Institute of Technology School of Civil and Water Resources Engineering for allowing me to use water quality and treatment laboratory.

I can't imagine finishing my study without the love, kindness, caring, encouragement, support and burden sharing from my beloved wife Mulu Bogale. Thank you and love you Muliye yene konjoo. My thanks also go to my family (Aanna, Etiye, Ayu, Yirgu, Fev, Kidu, Fina, Beru and Dibo) for their prayer, love and encouragement.

I would like also to thank all Habesha community at Enschede especially my batch (Asme, Edu, Fiker, Fre, Lozi, Mafi, Mahi, Maste, Micky, Mule, Sari, Tg (kecho) and Zola) and appreciate a friendship I had with all of them.

Last but not least, I thank my class mates (Amr, Asmelash, Chenyang, Edika, Jonathan, Mastawesha, Mahmoud, and Xin) for the precious and wonderful time we had together.

TABLE OF CONTENTS

Abstract	i
Acknowledgements	ii
List of Figures	v
List of tables	vi
Notations	vii
Abbreviations	viii
1. Introduction	1
1.1. Research Problem	2
1.2. Research Objective	2
1.3. Research and Technical Questions	2
2. Study Area	3
2.1. General	3
2.2. Climate of Lake Tana Basin	3
2.3. Geology of Lake Tana	3
2.4. Socioeconomic Factor of Lake Tana	3
2.5. Pervious Studies on Lake Tana by ITC	4
3. Literature Review	5
3.1. Inherent and Apparent Optical Properties	5
3.2. Optically Significant Constituents of Natural Waters	5
3.2.1. Total Suspended Matter (TSM)	6
3.2.2. Coloured dissolved organic matter (CDOM)	6
3.3. Hydro-Optical Models to Estimate the IOPs	6
4. Method	7
4.1. Field Measurements	7
4.1.1. Water Quality Variables Measurement	7
4.1.2. Turbidity	8
4.1.3. Suspended Particulate Matter	8
4.1.4. Chlorophyll a	8
4.1.5. CDOM Concentration	9
4.2. Spectral Data Measurement	9
4.3. Landsat-8 Dataset	9
4.3.1. Landsat-8 images of Lake Tana	10
4.3.2. Conversion of DN of the Landsat-8 image to TOA Reflectance	11
4.4. Field Data arrangement to Retrieve Water Quality Variables	11
4.4.1. Data Interpolation	11
4.4.2. Full Ramses Data	11
4.4.3. Reduced Ramses Data	11
4.5. Ramses Spectral Data Analysis	13
4.5.1. Remote Sensing Water Leaving Reflectance	13

4.5.2. Downwelling Attenuation Coefficient	13
4.6. Atmospheric Correction Using Hydrosat Model.....	14
4.6.1. Top of Atmosphere Reflectance	14
4.6.2. The Reyleigh Scattering Reflectance.....	14
4.6.3. The Surface Specular Reflectance	14
4.6.4. Gaseous Transmittance.....	14
4.6.5. The Diffuse Transmittance	14
4.6.6. Deriving the Water Leaving Reflectance.....	14
4.7. Deriving Inherent Optical Properties and Water Quality Variables.....	16
4.8. Error Analysis.....	19
5. Results and Discussions.....	23
5.1. Results from In-situ Measurement and In-situ Data Analysis.....	23
5.1.1. Water Quality Variables from the Field Measurement.....	23
5.1.2. Downwelling Irradiance and Upwelling Radiance from the Field Measurement.....	24
5.1.3. Remote Sensing Water Leaving Reflectance from Ramses Data.....	24
5.1.4. Downwelling attenuation coefficients.....	25
5.1.5. IOPs Retrieved from In Situ Measurement (Hydro-Optical Model Inversion).....	26
5.2. Results from the Image Data.....	28
5.2.1. Atmospheric correction (From Hydrosat).....	28
5.2.2. Verification of Atmospheric correction.....	29
5.3. IOPs Derived from Landsat-8 image.....	32
6. Calibration, validation and Uncertainty.....	33
6.1. Calibration and Validation of IOPs.....	33
6.2. Validation of the Water Quality Variables	34
6.3. The Sources of Uncertainty	35
6.3.1. Data Uncertainty.....	35
6.3.2. Calibration Parameter Uncertainty of Landsat-8.....	36
7. Spatiotemporal Variability of Water Quality Indicators in Lake Tana	37
7.1. Dry season (24 April 2013)	37
7.2. The peak rainy season (24 July 2013)	38
7.3. The end of rainy season (26 September 2013)	38
7.4. Shortly after the end of rainy season (29 November 2013)	38
8. Conclusion and recommendation.....	43
8.1. Conclusion	43
8.2. Recommendation.....	44
List of References.....	45
Appendix 1. Atmospheric correction Method (HYDROSAT).....	49
Appendix 2. Water Quality Retrieval (HYDROSAT method)	50
Appendix 3. Relative Spectral Response (RSR)of Landsat-8	51

LIST OF FIGURES

Figure 1 Study Area, Lake Tana, Ethiopia (the left figure which shows Lake Tana, tributary Rivers and outflowing river (Blue Nile) is taken from Palstra et al. (2004) as modified by Vijverberg et al. (2009)).....	4
Figure 2 Locations of Field Measurement.....	7
Figure 3 Relative Spectral Response of Landsat-8.....	12
Figure 4 General flow chart of water quality retrieval method.....	19
Figure 5 Downwelling Irradiance (left)and Upwelling Radiance (right).....	24
Figure 6 Remote Sensing Water Leaving Reflectance	25
Figure 7 Downwelling Attenuation Coefficient	25
Figure 8 Absorption Coefficient of Phytoplankton from Ramses data.....	26
Figure 9 Absorption Coefficient of detritus and CDOM (the right figure shows the absorption coefficient of detritus and gelbstoff from full Ramses data (the wavelength started at 319 and ends at 950) and the left shows the absorption of detritus and gelbstoff from reduced Ramses data (the wavelength starts at 443nm and ends at 865nm)).....	27
Figure 10 Backscattering Coefficient of SPM (the left is from full Ramses data and the right is from reduced Ramses data). The difference between the left and the right figure is that, the left starts from 319nm and ends at 950 and it is useful to study the UV light attenuation by SPM. However, the right figure starts from 443nm and ends at 865 and it only gives information about light attenuation by SPM starting from blue region.....	28
Figure 11 Comparison between TOA, Atmospheric Corrected and In-situ measured Reflectances (2013/09/26).....	29
Figure 12 RMSE between field measured and atmospheric corrected reflectance.....	30
Figure 13 Difference between atmospheric corrected and field measured Rrs.....	30
Figure 14 Comparison between averaged TOA, verified atmospheric corrected and in-situ water leaving reflectances	31
Figure 15 Comparison of RMSE before and after verification.....	31
Figure 16 The IOPs derived from the matchup data of image (26 September 2013). (a) derived absorption coefficient of detritus and gelbstoff at 443nm versus measured SPM concentration and (b) the derived backscattering coefficient of SPM at 443nm versus measured SPM concentration.....	32
Figure 17 SIOPs and associated uncertainties	33
Figure 18 The relation between derived absorption coefficient of detritus and gelbstoff with measured CDOM (a-c) and SPM concentrations (d).....	34
Figure 19 Derived SPM versus Measured SPM concentration	35
Figure 20 The Water Leaving Reflectance at Band 1(atmospheric corrected) and Natural Colour Composite of Lake Tana (19 April, 24 July, 26 September, and 29 November 2013)	39
Figure 21 The Water Leaving Reflectance (Atmospheric corrected) at Band 5 (19 April, 24 July, 26 September, and 29 November 2013 from left to right)	39
Figure 22 the absorption of detritus and gelbstoff at 443nm for the images of dry period, peak rainy season, end of rainy season, and shortly after the end of rainy season from left to right.	40
Figure 23 the backscattering coefficient of suspended particulate matter of Lake Tana for four different periods. Dry period, peak rainy season, end of rainy season and shortly after the end of rainy season from left to right.	41

LIST OF TABLES

Table 1 the spectral bands and their wavelengths of Landsat-8.....	10
Table 2 Landsat-8 data product	10
Table 3 Results from approach 2.....	12
Table 4 Results from approach 3.....	13
Table 5 Water Quality Variables Measured in the Field	23
Table 6 Absorption Coefficient of Phytoplankton from Ramses data.....	26
Table 7 The relation between the derived IOPs by considering the phytoplankton absorption with their respective measured concentrations.....	27
Table 8 Relation between Atmospheric Corrected and In-situ Measured Reflectance	29
Table 9 RMSE and rRMSE before and after verification.....	32
Table 10 Calibration and Validation outputs.....	33
Table 11 The wavelength range of TriOS Ramses data to work with Landsat-8's OLI bands.....	43

NOTATIONS

$a(\lambda)$	Bulk absorption Coefficient [m^{-1}]
$a_{dg}(\lambda)$	Absorption coefficient of detritus and gelbstof [m^{-1}]
A_f	The area of the filter [m^2]
$a_{micro}(\lambda)$	The shapes corresponding to absorption spectral for microphytoplankton
$a_{ph}(\lambda)$	Absorption coefficient of phytoplankton [m^{-1}]
$a_{pico}(\lambda)$	The shapes corresponding to absorption spectral for picophytoplankton
$a_w(\lambda)$	Absorption coefficient of water molecules [m^{-1}]
A_q	Band-specific additive rescaling factor
$b_b(\lambda)$	Bulk Backscattering coefficient [m^{-1}]
$b_w(\lambda)$	Backscattering coefficient of water molecules [m^{-1}]
$b_{bp}(\lambda)$	Backscattering coefficient of suspended particulate matter [m^{-1}]
$b_{b,spm}(\lambda)$	Backscattering coefficients suspended particulate matter [m^{-1}]
$c(\lambda)$	The beam attenuation coefficient [m^{-1}]
$E_d(\lambda)$	Downwelling irradiance [$W m^{-2}nm^{-1}$]
$K_d(\lambda)$	Average downward irradiance attenuation coefficient [m^{-1}]
$L_u(\lambda)$	Upwelling water leaving radiance [$W m^{-2}sr^{-1}nm^{-1}$]
$M_q(\lambda)$	Band-specific multiplicative rescaling factor []
$OD(\lambda)$	The optical density (absorbance)at selected wavelength []
$Q_{cal}(\lambda)$	Quantized and calibrated standard product pixel values (DN)
$R_{rs}(\lambda)$	Remote sensing water leaving reflectance [sr^{-1}]
s	The spectral exponent for absorption of detritus and gelbstoff [μm^{-1}]
S_f	The size parameter of phytoplankton
$T_g(\lambda)$	The gaseous transmittance
$T_v(\lambda)$	The viewing diffuse transmittance from water to sensor []
V_f	The volume of filtered sample [m^3]
Y	Spectral slope for particulate backscattering []
$\rho_a(\lambda)$	Aerosol scattering []
$\rho_r(\lambda)$	Reyleigh or molecular scattering []
$\rho_{sfc}(\lambda)$	The surface specular reflectance []
$\rho_t(\lambda)$	The total reflectance received by the sensor at TOA []
$\rho_w(\lambda)$	The water leaving reflectance []
$\rho(\lambda)$	TOA planetary reflectance []
θ_{SE}	Local sun elevation angle [Rad]
θ_{SZ}	Local solar zenith angle [Rad]
$\mathcal{E}_{(s,l)}$	Aerosol ratio between the short (s)and the long (l) wavelengths []
$\omega(\lambda)$	The single scattering albedo []
λ	Wavelength [μm or nm]
σ	Standard Deviation
δ	Exponent of Aerosol Ratio for wave length i ($i < s < l$)

ABBREVIATIONS

AOP	Apparent Optical Property
AC	Atmospheric Corrected
Chl-a	Chlorophyll a pigment
CDOM	Coloured Dissolved Organic Matter
IOP	Inherent Optical Property
NIR	Near Infra Red
OD	Optical Density
SIOP	Specific Inherent Optical Property
SPM	Suspended Particulate Matter
TOA	Top Of Atmosphere
GF/F	Glass Fiber/Filter
RMSES	Radiation Measurement Sensor with Enhanced Spectral Resolution
LDCM	Landsat Data Continuity Mission
OLI	Operational Land Imager
TIRS	Thermal Infrared Sensor
VNIR	Visible Near Infra Red
SWIR	Short Wave Infra Red
GloVis	Global Visualization Viewer
DN	Digital Number
USGS	United States Geological Survey
GeoTIFF	Geostationary Earth Orbit Tagged Image File Format
UTM	Universal Transverse Mercator
WGS 84	World Geodetic System 1984
NTU	Nephelometric Turbidity Unit
GPS	Global Positioning System
UV	Ultra Violet
TSM	Total Suspended Matter
RSR	Relative Spectral Response
CA	Costal Aerosol
RMSE	Root Mean Square Error
MAE	Mean Absolute Error
rRMSE	relative Root Mean Square Error

1. INTRODUCTION

Inland lakes are endangered by heavy sediment loads, eutrophication, and heavy metals and their quality has been degraded. The degradation of the lakes water quality is a major problem and concern and received lots of attention in the scientific community. In developing country like Ethiopia there is lack of researches to deal with water quality problems of the lakes. Concerning the hydrology of Lake Tana, the largest lake in Ethiopia, some of the examples of the studies which have been done can be mentioned (Kebede et al., 2006; Rientjes et al., 2013; Rientjes et al., 2011; Setegn et al., 2011; Setegn et al., 2009; Wale et al., 2008). However, regarding remote sensing of water quality very few studies have been reported. For example the suitability of MODIS TERRA image to determine sediment concentration has been evaluated by Ayana (2013). Even though Lake Tana is of significant importance to Ethiopia and the downstream countries (Sudan and Egypt) concerning the water resources aspect and the ecological balance of the area, its quality and quantity are deteriorating due to rapid growth of human population, soil erosion, sedimentation and eutrophication by organic and inorganic fertilizers from agricultural field (Setegn, 2010; Vijverberg et al., 2009). The most important factors affecting the lakes water quality in Ethiopia is human factors.

The sustainable management of fresh inland water systems requires the regular monitoring and assessments of water quality. However, the conventional water quality measurement techniques are limited in their spatial and temporal coverage, expensive and time consuming. Measuring the water quality of inland lakes requires systematic advanced instrumentation. Using remote sensing based water quality data in conjunction with accurately measured field water quality data give reasonable and accurate optically significant constituents of water (Dekker et al., 2001; Salama et al., 2009). To determine the existing status of water quality and to avoid the future water catastrophe, assessing and monitoring water quality using remote sensing in conjunction with in-situ measurement plays a significant role (Salama et al., 2009). However, in relation to the use of in-situ measurement and remote sensing observation there are constraints. The major constraints are lack of reliable retrieval algorithms in inland waters, the cost of hyperspectral optical satellite data and the equipment for in-situ measurements of water quality parameters (GEOSS, 2007). The constraints are exaggerated for most of the developing countries like Ethiopia which are characterized by lack of sustainable infrastructure in both human capacity and physical operational earth observation and in-situ observing system. Since the remote sensing of water quality to assess the quality of inland lakes is relatively new, further scientific studies still have to be done.

Remotely sensed data provide synoptic information of water quality at high temporal frequency (Salama et al., 2009). A derivation of inherent optical properties (IOPs) from remote sensing reflectance is commonly based on modelling (Gordon et al., 1988b), which aim to describe the relationship between remote sensing reflectance and the inherent optical properties (IOPs). IOPs of natural waters including absorption coefficient from water molecules, phytoplankton pigments, detritus and dissolved organic matter and backscattering coefficient from water molecules and suspended particulate matters are the most significant parameters governing the light propagation within the water column (Li et al., 2013; Maritorena et al., 2002; Salama et al., 2009). Morel and Prieur (1977) showed that the water leaving reflectance is directly proportional to the backscattering coefficient and inversely proportional to the absorption coefficient. For this study the remote sensing data have been acquired from the recently launched Landsat Data Continuity Mission's (LDCM), Landsat-8.

Besides the remote sensing water quality data, field measurement is necessary to validate the adapted hydro-optical model. The field data is useful to assess the acceptable accuracy of the derived IOPs from hydro-optical inversion model. In this thesis study, the relationship between the derived IOPs and measured concentration was evaluated using calibration and validation of geophysical observation model of Salama et al. (2012a). In-situ measurements are carried out in selected areas of Lake Tana. For each in-situ sample, downwelling irradiance and upwelling radiance (to obtain remote sensing water leaving reflectance), concentration of suspended sediment, coloured dissolved organic matter (CDOM), turbidity and chlorophyll-a absorption were defined.

In this study the water quality indicators for data scarce Lake Tana region were derived from Landsat-8 images using in-situ measurement and a Hydro-optical inversion model (Hydrosat) developed by Salama et al. (2012b). The model has been modified to derive most common water quality indicators from the Landsat-8 images. Water quality indicators are absorption of chlorophyll-a, absorption of detritus and gelbstoff, and backscattering of suspended particulate matter. The mentioned water quality variables are those can be quantified from optical aerospace sensors in the visible range of the solar spectrum (Giardino et al., 2010). The accuracy of modified Hydrosat to derive IOPs was evaluated using the in-situ measured water quality data.

1.1. Research Problem

The sustainable management of Lake Tana water requires the regular monitoring and assessments of water quality. However, there are constraints which have to be addressed in order to monitor the quality of the Lake Tana. Due to the limitation of the spatial and temporal coverage of the conventional water quality measurement techniques and lack of the retrieval algorithm of Lake Tana water quality from the recent remote sensing observation, there is no data available on water quality indicators of the lake. The spatiotemporal distribution of Lake Tana water quality indicators is not fully addressed.

1.2. Research Objective

The main objective of this study is to derive most common water quality indicators from Landsat-8 images in Lake Tana using in-situ measurements and hydro-optical model inversion and analyse their spatiotemporal variability. The Specific objectives are to:

- modify the Hydrosat model to derive water quality indicators from Landsat-8;
- develop an atmospheric correction scheme for Landsat-8

1.3. Research and Technical Questions

1. What is the current status of Lake Tana water quality?
2. How are the water quality variables distributed in space and time?
3. What is the most dominant water quality indicator of Lake Tana?
4. How to improve the Hydrosat model to retrieve water quality variables of Lake Tana using Landsat-8 images?
5. Is the spectral setup of Landsat-8 sufficient to improve the accuracy of retrievals?

2. STUDY AREA

2.1. General

Lake Tana is located at the northwest highlands' of Ethiopia at latitude 12°0' N and longitude 37°15' E in Amhara Region at an elevation of around 1800m amsl. It is a shallow Lake with a mean depth of 9m and maximum depth of 15m (Kaba Ayana, 2007); covers the drainage area of 15096km² (Setegn et al., 2011) with its surface area between 3000 to 3600km²; around 84km length and 66km width. The Lake is fed by more than 40 tributary rivers (Kebede et al., 2006; Wale et al., 2008). Rientjes et al. (2011) show that main rivers Gilgel Abay, Kelti, and Koga from the south, Gumara and Rib from the east, and Megech from the north contribute the majority of the inflow. Lake Tana is Ethiopia's largest lake, containing half the country's fresh water resources (Vijverberg et al., 2009), the third largest lake in the Nile Basin and is the source of the Blue Nile river. The area around the lake has been cultivating for the centuries. Most of the Lake Tana catchment is characterized as cropland with scarce woodlands while few limited areas which is less than 1% of the catchment area of highlands are forested (Wale, 2008). Mainly maize and rice cropping is carried out in the wetland adjacent to the lakeshore. The sediment loads from the tributary rivers as well as the nutrient loads from the agricultural areas and the nearby city are the major sources for the deterioration of the lake water quality.

2.2. Climate of Lake Tana Basin

The Lake Tana basin is located near the equator and its climate is typical of semi-arid regions. The annual rainfall pattern divided in to wet and dry season. The wet season mainly occurs from the month of June to September and the dry season from October to April (Minale & Rao, 2011). The wet season further divided in to minor rainy season (April and May) and major rainy season (June to September). Regarding the distribution of the rain, slightly more rain falling in the south and southeast than in the north of the lake catchment (Alemayehu et al., 2009). In general, the southern part of Lake Tana basin is wetter than the western and the northern parts (Kebede et al., 2006). The diurnal temperature varies between 30°C during day time and 6°C night time (Vijverberg et al., 2009). However, the mean annual temperature is about 20°C (Kebede et al., 2006; Wale, 2008).

2.3. Geology of Lake Tana

The Lake Tana is located in a wide depression of Ethiopian basaltic plateau and surrounded by the wetland all around the lake except in the northeast. The lake is bordered by flood plains that are often flooded during the rainy season such as Fogera floodplain in the east (associated with Gumara and Rib Rivers), Dembia floodplain in the north (associated with Megech River) and Kunzila floodplain in the southwest (associated with Gilgel Abay River, Kelti and Koga) and by steep rocks in the west and northwest (Vijverberg et al., 2009).

2.4. Socioeconomic Factor of Lake Tana

The total population in Lake Tana was estimated to be in excess 3 million (Alemayehu et al., 2009). This included the largest city on the lake shore, Bahir Dar, which has population of more than 200,000. At least 15,000 people live on the 37 islands in the lake. The lake is an important source of fish for the people around the lake and elsewhere in the country. In addition the lake region has high tourist attraction and the area is an important tourist destination in the country. The livelihood of more than five hundred thousand people directly or indirectly depends on the lake and adjacent wetlands (Vijverberg et al., 2009). The Lake Tana region has become the center of interest for Ethiopia's water resources development. Therefore, the Tana-Beles project has been constructed by transferring of water from Lake Tana to the

Beles river to generate hydropower with generating capacity of 460MW by exploiting the 311m elevation difference between the lake and the Beles river. In addition to the hydropower development, a number of irrigation schemes have been planned on the main rivers flowing into Lake Tana (Alemayehu et al., 2009).

2.5. Pervious Studies on Lake Tana by ITC

Students from the Faculty of Geo-Information Science and Earth Observation of the University of Twente (ITC) have done a lot of research on Lake Tana and some of them are mentioned hereafter. The level of Lake Tana using radar altimetry has been assessed and evaluated by Kaba Ayana (2007). The Hydrological balance of the lake was simulated by Wale (2008) giving emphasis for ungauged river inflows. Abreham Kibret (2009) estimated the open water evaporation from the lake using in-situ measurement in combination with MODIS/Terra imagery. The water balance of the lake has been simulated by Upul Janaka Perera (2009) and the gauged catchment river inflow, ungauged catchment river inflow, rainfall of lake area, open water evaporation of the lake, and the lake outflow were estimated as 1254, 527, 1347, 1563, and 1480mm/year, respectively. The impact of climate change on the lake water balance was assessed by Gebremariame (2009) and also Nigatu (2013) investigated the hydrological impact of climate change on the water balance of the lake. All the above mentioned studies were done focusing on the hydrology of the lake. The remote sensing based water quality of Lake Tana wasn't studied yet by ITC students.

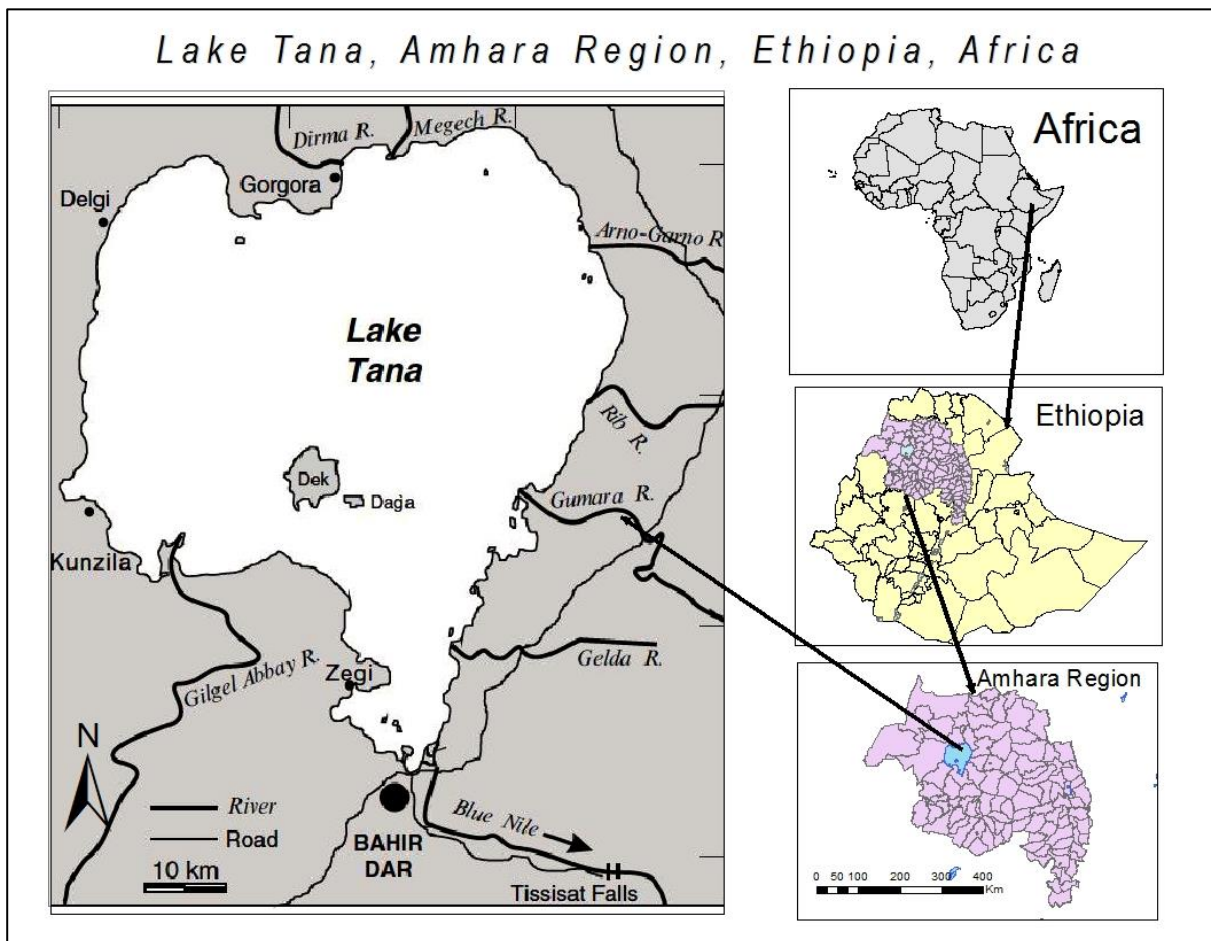


Figure 1 Study Area, Lake Tana, Ethiopia (the left figure which shows Lake Tana, tributary Rivers and outflowing river (Blue Nile) is taken from Palstra et al. (2004) as modified by Vijverberg et al. (2009))

3. LITERATURE REVIEW

3.1. Inherent and Apparent Optical Properties

Inherent optical properties (IOPs) are the optical properties of water which are independent of the ambient light field within the medium but only depend on the medium (Mobley, 2004). For open water bodies these properties include absorption ($a_{(\lambda)}$) and backscattering ($b_{b(\lambda)}$) coefficients which are the most significant parameters governing the light propagation within a water column (Gordon et al., 1975; Li et al., 2013; Mobley, 2004). In addition to these principal IOPs there are other IOPs which include the index of refraction, the beam attenuation coefficient and the single-scattering albedo. The beam attenuation coefficient ($c_{(\lambda)}$) is the sum of absorption ($a_{(\lambda)}$) and backscattering ($b_{b(\lambda)}$) coefficients :

$$c_{(\lambda)} = a_{(\lambda)} + b_{b(\lambda)} \dots\dots\dots 3.1$$

The single scattering albedo ($\omega_{(\lambda)}$) is characterized as:

$$\omega_{(\lambda)} = \frac{b_{b(\lambda)}}{a_{(\lambda)}} \dots\dots\dots 3.2$$

Apparent optical properties (AOPs) are the optical properties of water which depend on the directional structure of the ambient light field and on the medium (Mobley, 2004). These apparent optical properties include irradiance, radiance, irradiance reflectance, remote sensing reflectance, diffuse attenuation coefficient and average cosines. Irradiance is the radiant energy per time, per area and per wavelength ($W m^{-2} nm^{-1}$) and can vary highly in magnitude in a fraction of time if a cloud passes in front of the sun (Mobley, 2004). Radiance indicates directional, temporal, spatial, and wavelength structure of the light field and is the radiant energy per area, per time, per solid angle and per wavelength ($W m^{-2} nm^{-1} sr^{-1}$) (refer section 5.1.2 for the field measured irradiance and radiance of this study). Irradiance reflectance (ratio of irradiance) is one of commonly used AOP that is ratio of upwelling irradiance to downwelling irradiance. Average cosine is another commonly used AOP which depends on the structure of the light field. Upwelling or downwelling average cosine is the ratio of upwelling or downwelling irradiance to the upwelling or downwelling all-directional total irradiance event at a point (scalar irradiance) (Mobley, 2004). The remote sensing reflectance and diffuse attenuation coefficient are discussed in sections 4.5.1 and 4.5.2 respectively and their field measurement results and discussion are carried out in section 5.1.3 and 5.1.4.

3.2. Optically Significant Constituents of Natural Waters

As it has been discussed in detail by Mobley (2004) water is composed of dissolved (when filtering passes through 0.2 μm pore) and particulate (when filtering retained on 0.4 μm pore) matter of organic and inorganic origins, living and non-living. Each of these components of natural waters contributes in one or in another way to the values of optical properties of a given water body. Basically the most important optically significant constituents of natural waters which contribute to IOPs are water molecules, Chlorophyll-a, detritus and dissolved organic matter and suspended particulate matter. Based on the abundance of these constituents, Morel and Prieur (1977) classified open water bodies in to two cases. According to their classification Case 1 is that all water constituents are function of phytoplankton whereas in Case 2 water constituents vary independent of each other. In both cases dissolved yellow substance contributes to total absorption and is present in variable amounts.

3.2.1. Total Suspended Matter (TSM)

Total suspended matter or suspended particulate matter expresses the concentration of inorganic or organic particles which are suspended in water. Inorganic particles mainly are soil particles. The organic particles are created as bacteria, phytoplankton, and zooplankton grow and reproduce. Phytoplankton cells are strong absorbers of visible light and therefore play a major role in determining the absorption properties of natural waters. Phytoplankton absorption is mainly due to photosynthetic pigments and characterized by strong absorption bands in the blue and in the red with very little absorption in the green. The absorption of phytoplankton has been studied and the peaking absorption wavelengths in these strong absorption bands are reported in different literatures (Briucaud et al., 1981; Lindell et al., 1999; Mobley, 2004; Morel & Prieur, 1977).

Inorganic particles are created primarily by weathering of terrestrial rocks and soils. Particles can enter the water body as wind-blown dust settles on the water surface, as suspended sediment load of rivers that carry the eroded soil particles, or as currents re-suspend bottom sediments. In lakes or reservoirs sediment loads may indicate a soil erosion problems from contributing watershed (Ritchie et al., 1987). Suspended particulate matter usually is the major determiner of both the absorption and scattering properties of natural waters and is responsible for most of the temporal and spatial variability in these optical properties (Mobley, 2004). It is a measure of water turbidity and directly affects the light distribution in a water column.

3.3. Coloured dissolved organic matter (CDOM)

CDOM is one of the major light absorbing constituent in natural water and found in all natural water (Stedmon et al., 2000); also called yellow substance. The dissolved yellow substance in inland water is generated by decomposition of plant matter within the water and soluble humic substances leached from the soil in the catchment area (indirectly from the vegetation)(Kirk, 1994). Its light absorption increases with decreasing wavelength and consists of dissolved and colloidal organic compounds which are responsible for the absorption of light mostly in ultraviolet (UV) region and in addition to pigments and non-living materials it is one of the factor that determines the shape of the total absorption in the visible range (Briucaud et al., 1981; Morel & Prieur, 1977).

3.4. Hydro-Optical Models to Estimate the IOPs

The IOPs of the water can be estimated by inverting hydro-optical models. The most widely used hydro-optical model is a semi-analytical surface water model developed by Gordon et al. (1988b). This model relates the normalized water-leaving radiance to the optical properties of the water and its constituents. With a simple modification and parameterization, this model has been adapted and IOPs of water were retrieved from different parts of the world with a reasonable accuracy (Garver & Siegel, 1997; Maritorena et al., 2002; Salama et al., 2009; Salama et al., 2012b; Salama & Shen, 2010). Another semi-analytical model is a shallow water model developed by Lee et al. (1998) and Lee et al. (1999). This model assumed the subsurface remote sensing reflectance as the approximated sum of a deep water signals and a bottom signal.

The hydro-optical model (Hydrosat) developed by Salama et al. (2012b) has been used in this study. The Hydrosat is a region and time independent remote sensing model that derives all possible water quality variables from Landsat images and does not require tuning with field measurements (Salama et al., 2012b). The method and the parameterizations followed in this study are discussed and presented in sections 4.6 and 4.7.

4. METHOD

4.1. Field Measurements

The field measurements were carried out in September 2013 which is at the end of rainy season. At five measurement days 79 sample points were visited and water samples were taken. The days were selected based on the satellites over pass. Landsat-8 passed over the lake on the 10th and 26th of September 2013 and Landsat-7 passed in 18th of September 2013. The first two days (9th and 10th of September 2013) were completely cloudy. The other days 18th, 20th and 26th of September 2013 were free of cloud. The measurements cover the area between the lake inlet of Gumara river and the lake outlet of the Blue Nile river at Bahir Dar. The measurements' distance between each two consecutive points ranged from 500 to 1000m within the time period of 9:45AM - 11:30 AM (Landsat-8 passes over the lake around 10:50AM). The total measurement distance covered around 40km. Within the short period of field measurement, performing measurements across the entire Lake (around 3600km²) was not possible. Therefore, the measurements were taken in the area which could relatively easy be accessed by locally available boats at the time the satellites overpassed the lake. The average time for the boat from the port (Bahir Dar) to arrive to the Gumara river inlet was 4 hours. The positions of the sampling points were recorded by using GPS. The points where the samples were collected for laboratory analysis and the simultaneous field measurements were taken place have been shown in Figure 2.

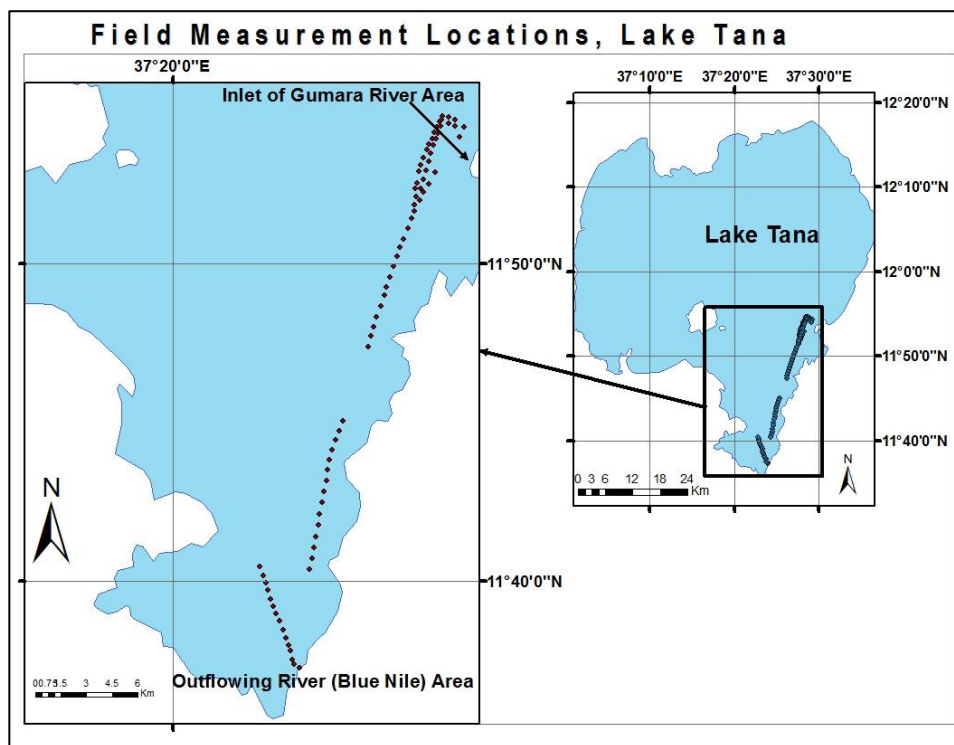


Figure 2 Locations of Field Measurement

4.1.1. Water Quality Variables Measurement

Water samples were collected for TSM, Turbidity and Chlorophyll-a analysis. From each sampling point, one litre of the water sample was collected from the upper level of approximately 20cm and the measurements were performed between three to four hours of the last sample collection. The Samples were analysed at Bahir Dar University Institute of Technology in Water Quality and Treatment Laboratory.

4.1.2. Turbidity

Turbidity was measured in the laboratory by using turbidity meter. The equipment was calibrated by using provided standards from 0.1 to 7500 NTU. After calibrating the turbidity meter, the turbidity of the samples was measured by shaking the samples well and inserting the sample tube in the meter.



4.1.3. Suspended Particulate Matter

Suspended Particulate matter (SPM) was measured by using gravimetric analysis. The apparatus which were used to determine SPM by gravimetric method are: electronic balance, vacuum pump, filtration system, oven, desiccators, graduated cylinder, filter paper, forceps for handling filter paper and distilled water. The measured volume of water samples (100ml for turbid and 200ml for relatively clear water) was filtered through the pre-weighed dry Whatman GF/F filters of pore size 0.45µm. To dissolve soluble salts the distilled water of volume 200ml was passed through the filter. The filters were removed from the filtration unit and dried in the oven. After cooling the dried filters at room temperature in desiccator, the filters were weighted by using electronic balance. The electronic balance which was used for this measurement can measure three digits after decimal in gram. Therefore the gram has been converted in to milligram and the following formula was used to determine SPM concentration within a given volume of liquid in mg/l.

$$Total\ suspended\ solid\ \left(\frac{mg}{l}\right) = \frac{(final\ weight\ (mg) - original\ weight\ (mg)) \times 1000}{sample\ volume\ (ml)} \dots \dots 4.1$$



4.1.4. Chlorophyll a

The absorption of chlorophyll-a was measured by adapting the ocean optics protocols from Fargion and Mueller (2000). The phytoplankton pigment was extracted from the collected sample after 3 - 4 hours of last sample collection. The 200ml sample was filtered through Whatman glass fiber filter (GF/F) of

0.45µm and the filter was grinded by using 90% aqueous acetone solution to extract the pigment. The grinded filter sample was transferred to centrifuge tube and it was centrifuged for 30 minutes at 2500rpm. The clarified extract was transferred to a 1cm cuvette and optical density (OD) was read at different wavelength by using spectrophotometer. The chlorophyll-a absorption coefficient was determined by using the equation from Fargion and Mueller (2000) as;

$$a_{ph(\lambda)} = 2.303 * (OD_{(\lambda)} - OD_{(750)}) * \frac{A_f}{V_f} \dots \dots \dots 4.2$$

Where A_f is the area of the filter [m²], V_f is the volume of filtered sample [m³] and $OD_{(\lambda)}$ is the optical density (absorbance) at selected wavelength. The $OD_{(750)}$ was used to correct for the scattering effect.



4.1.5. CDOM Concentration

CDOM concentration was measured by microFlu-CDOM fluorometer in µg/l. The microFlu-CDOM fluorometer is a low-cost miniaturized submersible fluorometer for high precision and selective CDOM (Coloured Dissolved Organic Matter, "Yellow matter", "Gelbstoff") fluorescence measurements. The combination of a greatly reduced scale design with long-term stability makes it suitable for yellow substance monitoring applications in lakes and rivers as well as for all applications in the field of water quality and waste water monitoring (<http://www.trios.de/>).

4.2. Spectral Data Measurement

The radiometric measurements were performed using TriOS-RAMSES (Radiation Measurement Sensor with Enhanced Spectral Resolution) hyperspectral spectroradiometer, one (TriOS RAMSES-ACC-VIS irradiance sensor) measuring downwelling irradiance ($Ed(\lambda)$) and one (TriOS RAMSES-ARC radiance sensor) measuring upwelling radiance($Lu(\lambda)$). The sensors measure in the spectral range from 318 to 951nm with sampling interval of approximately 3.3nm. The radiometric data were collected at the five measurement days from 79 sample points and was simultaneously taken when water samples were taken. In each measurement point the spectral measurements were carried out in three positions such as just above the water, 10 cm and 50 cm under the water.

4.3. Landsat-8 Dataset

The Landsat Data Continuity Mission’s (LDCM), Landsat-8, is the latest satellite, which has been launched in 11th of February 2013 and images the entire earth every 16 days in an 8-day offset from Landsat-7 and consists of two sensors namely, Operational Land Imager (OLI) and Thermal Infrared Sensor (TIRS). The OLI instrument images the earth in 9 spectral bands which cover the visible, near-Infrared (VNIR) and Short Wave IR (SWIR) portions of the electromagnetic spectrum. The two new spectral bands which have been added are a deep-blue band for coastal water and aerosol studies (band 1), and a band for cirrus cloud detection (band 9). All OLI bands are acquired at 12-bit radiometric resolution; 8 bands are acquired

at 30 meters spatial resolution and 1 band, the panchromatic band, is acquired at 15 meters spatial resolution. The TIRS collects data in two long wavelengths which are the thermal infrared bands 10 and 11. The 100-meter spatial resolution of TIRS data is registered to the OLI data to create radiometrically and geometrically calibrated, terrain-corrected 16-bit Level 1 data products. These two TRIS bands are useful in providing more accurate surface temperatures (<http://pubs.er.usgs.gov/publication/fs20133060>). The spectral bands of Landsat-8 and their corresponding wavelengths are presented in Table 1.

4.3.1. Landsat-8 images of Lake Tana

Eleven cloud free images of path 170 and row 052 from April to November 2013 have been downloaded from GloVis (<http://glovis.usgs.gov/>). These images were processed in ENVI + IDL. The OLI bands of the images have been stacked together, and the Lake Tana area has been subset via the selected region of interest. On the subset images the conversions from DN to reflectance, the first haze correction, and atmospheric correction were performed. The data received from Landsat-8 were processed using parameters consistent with all standard Landsat data products shown in Table 2.

Table 1 the spectral bands and their wavelengths of Landsat-8

	Wavelength (μm)	Band center (nm)	Resolution (meters)
Band 1 - Coastal aerosol (OLI)	0.43 - 0.45	443	30
Band 2 – Blue (OLI)	0.45 - 0.51	482	30
Band 3 – Green (OLI)	0.53 - 0.59	562	30
Band 4 – Red (OLI)	0.64 - 0.67	655	30
Band 5 - Near Infrared (NIR) (OLI)	0.85 - 0.88	865	30
Band 6 - SWIR 1 (OLI)	1.57 - 1.65	1610	30
Band 7 - SWIR 2 (OLI)	2.11 - 2.29	2200	30
Band 8 – Panchromatic (OLI)	0.50 - 0.68	590	15
Band 9 – Cirrus (OLI)	1.36 - 1.38	1372	30
Band 10 - Thermal Infrared (TIRS) 1	10.60 - 11.19	10800	100
Band 11 - Thermal Infrared (TIRS) 2	11.50 - 12.51	12000	100

Table 2 Landsat-8 data product

Product Type	Level 1T (terrain corrected)
Data type	16-bit unsigned integer
Output format	GeoTIFF
Pixel size	15 meters/30 meters/100 meters (panchromatic/multispectral/thermal)
Map projection	UTM (Polar Stereographic for Antarctica)
Datum	WGS 84
Orientation	North-up (map)
Resampling	Cubic convolution
Accuracy	OLI: 12 meters circular error, 90 percent confidence TIRS: 41 meters circular error, 90 percent confidence

4.3.2. Conversion of DN of the Landsat-8 image to TOA Reflectance

The Digital Number (DN) value of the collected image has been converted to the top of atmosphere planetary reflectance using rescaling coefficients provided in the image’s metadata file. The equation to covert DN of the image to TOA planetary reflectance has been obtained from USGS website (http://landsat.usgs.gov/Landsat8_Using_Product.php) as;

$$\rho(\lambda) = \frac{(M_{\rho(\lambda)}Q_{cal(\lambda)} + A_{\rho})}{\cos(\theta_{SZ})} = \frac{(M_{\rho(\lambda)}Q_{cal(\lambda)} + A_{\rho})}{\sin(\theta_{SE})} \dots \dots \dots 4.3$$

Where; $\rho(\lambda)$ is TOA planetary reflectance, M_{ρ} is band-specific multiplicative rescaling factor from the metadata (REFLECTANCE_MULT_BAND_x, where x is the band number) , A_{ρ} is band-specific additive rescaling factor from the metadata (REFLECTANCE_ADD_BAND_x, where x is the band number), Q_{cal} is quantized and calibrated standard product pixel values (DN), θ_{SE} is local sun elevation angle. The scene center sun elevation angle in degrees is provided in the metadata (SUN_ELEVATION). θ_{SZ} is local solar zenith angle; $\theta_{SZ} = 90^{\circ} - \theta_{SE}$

4.4. Field Data arrangement to Retrieve Water Quality Variables

4.4.1. Data Interpolation

Ramses data are first interpolated to 1nm interval. The need to interpolate Ramses data in 1nm interval is to simulate the Landsat-8 spectral response as the relative spectral responses (RSR) of Landsat-8 were given in 1nm interval.

4.4.2. Full Ramses Data

The Ramses data has been arranged for the wavelengths from 400nm to 700nm and from 319nm to 950nm with 1nm interval for the retrieval of the water quality variables. To retrieve all remotely sensed water quality variables Ramses data from wavelengths 400nm to 700nm were used (301 bands). The wavelengths limitation within this range was because of the spectral range of absorption of chlorophyll-a. The shapes values of the smallest and largest cells for chlorophyll-a absorption analysis are provided for wavelengths from 400 to 700nm only (refer section 4.7). However the water quality variables also were retrieved by using the wavelengths from 319nm to 950nm in 1nm interval (632 bands). This data was used to retrieve other water quality variables by neglecting the spectral absorption of phytoplankton. The reason for neglecting the absorption from phytoplankton is that its concentration was very small at the period when the field measurements were performed (refer section 5.1.5). In this study the above two data sets have been called full Ramses data with and without phytoplankton absorption.

4.4.3. Reduced Ramses Data

The Ramses data has been reduced by following the relative spectral response (RSR) of Landsat-8 bands. The RSRs of Landsat-8 were obtained from the web (http://landsat.usgs.gov/tools_spectralViewer.php) and Ramses data was arranged based on it. From the RSR of Landsat-8 of each band we can see that there are differences in the observational response in band’s interval. For instance, the OLI’s costal aerosol (CA) band of Landsat-8 can observe in the wavelengths range from 427nm to 459nm. However, the spectral response in each wavelength is different from one another in this band. For the first (427 – 434) and the last (451 - 459) wavelengths the relative spectral response is nearer to zero and for the wavelengths from 436-450nm the RSR is greater than zero and nearer to one. For the other bands of Landsat-8 the RSR for some of their wavelengths is even recorded as negative (refer Appendix 3). Therefore, the Ramses data should be arranged by considering the relative spectral response of the

$$RSR_{mean} = \frac{1}{\Delta\lambda} \sum_{\lambda_1:RSR>0.9}^{\lambda_2:RSR>0.9} \Delta RSR \dots \dots \dots 4.5$$

Table 4 Results from approach 3

Bands	Wavelength range	Computed RSR	Central Wavelength
Costal Aerosol	436-450	0.957	443
Blue	454-511	0.928	482.5
Green	535-588	0.966	566.5
Red	637-672	0.964	654.5
NIR	852 - 877	0.951	864.5

The relationship between Ramses remote sensing reflectance values obtained by considering the RSR greater than zero (method 2) and greater than 0.9 (method 3) was computed. From the computation it has been seen that the RSR which has been obtained from approach 3 was twice of the RSR which has been obtained from approach 2 and 1 (Table 3 and Table 4). Therefore, for this study the reduced Ramses data obtained from the third approach has been used.

4.5. Ramses Spectral Data Analysis

4.5.1. Remote Sensing Water Leaving Reflectance

Remote sensing water leaving reflectance ($Rrs(\lambda)$) was computed by dividing upwelling water leaving radiance ($Lu(\lambda)$) to downwelling irradiance ($Ed(\lambda)$) just above the water surface (Mobley, 1999; Mobley, 2004) as:

$$Rrs(\lambda) = \frac{Lu(\lambda)}{Ed(\lambda)} \dots \dots \dots 4.6$$

The remote sensing water leaving reflectance is the most important quantity in remote sensing water quality to retrieve optically significant water quality constituents. The remote sensing water leaving reflectance (in inverse of Steradian (sr⁻¹)) of this study has been calculated using the field measured upwelling radiance and downwelling irradiance and the result has been presented in section 5.1.3.

4.5.2. Downwelling Attenuation Coefficient

The Downwelling attenuation coefficient was computed for all Ramses data using the following relation (Smith & Baker, 1981) as;

$$K_d(\Delta z, \lambda) = -\frac{1}{\Delta z} \ln \frac{E_d(z_2, \lambda)}{E_d(z_1, \lambda)} \dots \dots \dots 4.7$$

Where K_d is the average downward irradiance attenuation coefficient for a water column [m^{-1}], Δz is the thickness of the water column [m], E_d is the downwelling irradiance [$W m^{-2} nm^{-1}$]. The downwelling irradiances measured just above the water and at 50cm depth below the water surface were used to compute the downwelling attenuation coefficient at the depth of 50cm. The output from the analysis has been exhibited in section 5.1.4.

4.6. Atmospheric Correction Using Hydrosat Model

4.6.1. Top of Atmosphere Reflectance

At the top of atmosphere the total reflectance received by a sensor is the result of several components (Gordon, 1997) and it can be written as (Salama et al., 2012b):

$$\rho_{t(\lambda)} = T_{g(\lambda)} (\rho_{a(\lambda)} + \rho_{r(\lambda)} + T_{v(\lambda)}\rho_{sfc(\lambda)} + T_{v(\lambda)}\rho_{w(\lambda)}) \dots\dots\dots 4.8$$

Where $\rho_{t(\lambda)}$ is the total reflectance received by the sensor at wavelength λ , $T_{g(\lambda)}$ is the gaseous transmittance, $T_{v(\lambda)}$ is the viewing diffuse transmittance from water to sensor, $\rho_{a(\lambda)}$ is aerosol scattering, $\rho_{r(\lambda)}$ is air molecules scattering, $\rho_{sfc(\lambda)}$ is the surface specular reflectance and $\rho_{w(\lambda)}$ is the water leaving reflectance. Top of atmospheric reflectance has been obtained from Landsat-8 satellite images.

4.6.2. The Reyleigh Scattering Reflectance

One of the steps in the atmospheric correction procedure is the computation of the contribution of Reyleigh or molecular scattering ($\rho_{r(\lambda)}$) by atmosphere to top of atmosphere reflectance. The contribution of Reyleigh scattering to the total top of atmosphere reflectance is high (Gordon et al., 1988a) and has to be computed accurately. It has been computed by following Gordon et al. (1988a) approach from viewing illumination geometry and air pressure.

4.6.3. The Surface Specular Reflectance

From unpolarised light beam normally incident on still air-water surface about 2% of it will be reflected and about 98% will be transmitted in to the water below (Preisendorfer, 1976). The surface specular reflectance ($\rho_{sfc(\lambda)}$) was neglected.

4.6.4. Gaseous Transmittance

The signal received at the sensor level has been attenuated by gaseous absorption. The considered gases are ozone (absorption peak 0.43 - 0.75 μ m), oxygen (absorption peak 0.76 μ m), and water vapor (absorption peak 0.72, 0.82 and 0.94 and highly variable). The transmittance of any of these gases ($T_{g(\lambda)}$) is affected by its vertical and spatial distributions in the atmosphere. These gases, except water vapor, are uniformly mixed within each layer of the atmosphere and vary with in height, season and wavelength. Therefore, knowing the altitude, the season and water vapor content (for water vapor transmittance), their transmittance can be calculated by using the transmittance model of Goody (1964) and Malkmus (1967).

4.6.5. The Diffuse Transmittance

The diffuse atmospheric transmittance ($T_{v(\lambda)}$) is accountable for the effects of propagating water leaving reflectance from the water surface to the top of the atmosphere and it was approximated by using the model of Wang (1999) which has been modified from the Gordon et al. (1983).

4.6.6. Deriving the Water Leaving Reflectance

The water leaving reflectance ($\rho_{w(\lambda)}$) is the quantity of interest of remote sensing water quality and resulting from the interaction between the light and the water quality constituents in the water column. The water leaving reflectance was derived by following the method of Salama et al. (2004); Salama and Shen (2010), and Salama et al. (2012b) as;

$$(\rho_{a(\lambda)} + T_{v(\lambda)}\rho_{w(\lambda)}) = \frac{\rho_{t(\lambda)}}{T_{g(\lambda)}} - (\rho_{r(\lambda)} + T_{v(\lambda)}\rho_{sfc(\lambda)}) \dots\dots\dots 4.9$$

The right hand side of the above equation has been called the corrected reflectance ($\rho_{c(\lambda)}$) (Salama & Shen, 2010) and is represented as follows:

$$\rho_c(\lambda) = \frac{\rho_{t(\lambda)}}{T_{g(\lambda)}} - (\rho_{r(\lambda)} + T_{v(\lambda)}\rho_{f(\lambda)}) = \rho_a(\lambda) + T_{v(\lambda)}\rho_w(\lambda) \dots \dots \dots 4.10$$

$$T_{v(\lambda)}\rho_w(\lambda) = \rho_c(\lambda) - \rho_a(\lambda) \dots \dots \dots 4.11$$

The unknowns in the above equation (4.11) are aerosol reflectance and water leaving reflectance. The aerosol reflectance can be estimated from Landsat-8 bands by taking the aerosol ratio between the short and the long wavelengths as;

$$\epsilon_{(s,l)} = \frac{\rho_a(s)}{\rho_a(l)} \dots \dots \dots 4.12$$

From the above equation;

$$\rho_a(s) = \epsilon_{(s,l)} * \rho_a(l) \dots \dots \dots 4.13$$

The value of $\epsilon_{(s,l)}$ can be computed from the correlation between the corrected reflectance of band *s* and *l* (Salama et al., 2012b) of Landsat-8 as;

$$\epsilon_{(s,l)} = \cot \left[0.5 \tan^{-1} \left(\frac{c_{ll}}{c_{ss} - c_{sl}} \right) \right] \dots \dots \dots 4.14$$

Where *s* is the short wavelength (865nm); *l* is the long wavelength (1610nm); and *C* is the correlation between corrected reflectance of *s* and *l* bands of Landsat-8. The *C* value of *s* and *l* bands can be obtained from the statistics of the bands in ENVI + IDL.

The aerosol ratio ($\epsilon_{(s,l)}$) can also be extrapolated to find ($\epsilon_{(i,l)}$) for any other wavelengths (*i*) (Salama & Shen, 2010) as;

$$\epsilon_{(i,l)} = \epsilon_{(s,l)}^{\delta_i} \dots \dots \dots 4.15$$

$$\text{For } i < s < l \text{ where } \delta_i = \frac{(l-i)}{(l-s)} \dots \dots \dots 4.16$$

The water leaving reflectance for *s* band of Landsat-8 was computed from the above relations as;

$$\rho_{w(s)} = \frac{\rho_{c(s)} - \rho_a(s)}{T_{v(s)}} \dots \dots \dots 4.17$$

$$\rho_{w(s)} = \frac{\rho_{c(s)} - \epsilon_{(s,l)} * \rho_a(l)}{T_{v(s)}} \dots \dots \dots 4.17$$

The water leaving reflectance for other bands of Landsat-8 was computed as;

$$\rho_{w(i)} = \frac{\rho_{c(i)} - \rho_a(l) * \epsilon_{(s,l)}^{\delta(i)}}{T_{v(i)}} \dots \dots \dots 4.18$$

The purpose of atmospheric correction is to retrieve the water leaving reflectance. Deriving the water leaving reflectance (ρ_w) from the total received reflectance is conventionally called atmospheric correction. See Appendix 1 for the flow chart of atmospheric correction method.

4.7. Deriving Inherent Optical Properties and Water Quality Variables

The inherent optical properties were derived by inverting the semi-analytical model (Gordon et al., 1988b) and following the matrix inversion method developed by Hoge and Lyon (1996) and Wang et al. (2005). The water leaving reflectance ($\rho_w(\lambda)$) retrieved from atmospheric correction method (section 4.6) is converted into remote sensing reflectance (Rrs) as;

$$Rrs = \frac{\rho_w(\lambda)}{\pi} \dots\dots\dots 4.19$$

From the Gordon et al. (1988b) the remote sensing reflectance is related to IOPs as;

$$Rrs_{(\lambda)} = g_1 \left(\frac{b_{b(\lambda)}}{a_{(\lambda)} + b_{b(\lambda)}} \right) + g_2 \left(\frac{b_{b(\lambda)}}{a_{(\lambda)} + b_{b(\lambda)}} \right)^2 \dots\dots\dots 4.20$$

Where g_1 and g_2 are subsurface expansion coefficients; due to internal refraction, reflection and sun zenith and their values equal to 0.0949 and 0.0794 respectively. The parameters $b_{b(\lambda)}$ and $a_{(\lambda)}$ are the bulk backscattering and absorption coefficients of the water column, respectively.

The above equation (4.20) can be written as;

$$Rrs_{(\lambda)} = g_1 u_{(\lambda)} + g_2 u_{(\lambda)}^2 \dots\dots\dots 4.21$$

$$\text{Where, } u_{(\lambda)} = \frac{b_{b(\lambda)}}{a_{(\lambda)} + b_{b(\lambda)}} \dots\dots\dots 4.22$$

Equation 4.22 can be rearranged as:

$$u_{(\lambda)} * (a_{(\lambda)} + b_{b(\lambda)}) - b_{b(\lambda)} = 0$$

$$a_{(\lambda)} + b_{b(\lambda)} * \left(1 - \frac{1}{u_{(\lambda)}}\right) = 0$$

$$\text{Let } x_{(\lambda)} = 1 - \frac{1}{u_{(\lambda)}}$$

$$a_{(\lambda)} + b_{b(\lambda)} * x_{(\lambda)} = 0 \dots\dots\dots 4.23$$

The bulk absorption coefficient $a_{(\lambda)}$ is the sum of absorption of all contributing water constituents:

$$a_{(\lambda)} = a_{w(\lambda)} + a_{ph(\lambda)} + a_{dg(\lambda)} \dots\dots\dots 4.24$$

Where $a_{w(\lambda)}$ is the absorption of the water molecule, $a_{ph(\lambda)}$ is the absorption of phytoplankton, $a_{dg(\lambda)}$ is the absorption of detritus and gelbstoff. The absorption of water molecule can be taken from Pope and Fry (1997), Mobley (2004) or Smith and Baker (1981). The spectral absorption coefficient of phytoplankton $a_{ph(\lambda)}$ was parameterized by Ciotti et al. (2002) as a function of a size parameter describing the relative contributions of picophytoplankton and microphytoplankton as:

$$a_{ph(\lambda)} = a_{ph(0.44)} (s_f a_{pico(\lambda)} + (1 - s_f) a_{micro(\lambda)}) \dots\dots\dots 4.25$$

Where a_{pico} and a_{micro} are the shapes corresponding to the normalized absorption spectral for the smallest and largest cells and their values for the wavelengths from 400 to 700nm are provided in Ciotti et al. (2002), S_f is the size parameter varies between zero and one and 0.44 is the reference wavelength in μm where the phytoplankton (ph). The absorption coefficient of the combined effect of detritus and gelbstoff has been parameterized as (Briucaud et al., 1981; Wang et al., 2005);

$$a_{dg(\lambda)} = a_{dg(0.44)} \exp(-s(\lambda - 0.44)) \dots\dots\dots 4.26$$

Where s is the spectral exponent ranging between 0.008 and 0.03 and can be obtained from the literatures (Babin et al., 2003; Salama & Stein, 2009a; Wang et al., 2005).

The bulk backscattering coefficient is the sum of backscattering coefficients from water molecules and suspended particulate matter:

$$b_{b(\lambda)} = b_{b,w(\lambda)} + b_{b,spm(\lambda)} \dots\dots\dots 4.27$$

The backscattering coefficient of water molecules can be taken from Smith and Baker (1981) or Mobley (2004). The backscattering coefficient of suspended particulate matter (SPM) can be parameterized as (Haltrin & Kattawar, 1991):

$$b_{b,spm(\lambda)} = b_{b,spm(0.4)} \left(\frac{0.4}{\lambda}\right)^Y \dots\dots\dots 4.28$$

Where 0.4 is the reference wavelength in μm , Y is spectral slope for particulate backscattering and its value stated in literatures (Salama & Stein, 2009a; Wang et al., 2005) is in between 0 and 2.5.

Equation (4.23) can be rewritten as:

$$a_{w(\lambda)} + a_{ph(\lambda)} + a_{dg(\lambda)} + (b_{w(\lambda)} + b_{b,spm(\lambda)}) * x_{(\lambda)} \dots\dots\dots 4.29$$

By substituting equations from 4.25 to 4.28 in equation 4.29 we have gotten:

$$a_{w(\lambda)} + a_{ph(0.44)} (S_f a_{pico(\lambda)} + (1 - S_f) a_{micro(\lambda)}) + a_{dg(0.44)} \exp(-s(\lambda - 0.44)) + (b_{w(\lambda)} + b_{b,spm(0.4)} \left(\frac{0.4}{\lambda}\right)^Y) * x_{(\lambda)} = 0 \dots\dots\dots 4.30$$

The above equation can be rearranged as:

$$a_{ph(0.44)} (S_f a_{pico(\lambda)} + (1 - S_f) a_{micro(\lambda)}) + a_{dg(0.44)} \exp(-s(\lambda - 0.44)) + b_{b,spm(0.4)} \left(\frac{0.4}{\lambda}\right)^Y * x_{(\lambda)} = -(a_{w(\lambda)} + b_{bw(\lambda)} * x_{(\lambda)}) \dots\dots\dots 4.31$$

In equation 4.31 there are three unknowns (chlorophyll-a absorption coefficient at 440nm ($a_{ph(0.44)}$), absorption coefficient of detritus and gelbstoff at 440nm ($a_{dg(0.44)}$) and backscattering coefficient of suspended particulate matter at 400nm ($b_{b,spm(0.4)}$). To find solutions for these three unknowns we need at least three equations and written in terms of wavelengths as:

$$a_{ph(0.44)} (S_f a_{pico(\lambda_1)} + (1 - S_f) a_{micro(\lambda_1)}) + a_{dg(0.44)} \exp(-s(\lambda_1 - 0.44)) + b_{b,spm(0.4)} \left(\frac{0.4}{\lambda_1}\right)^Y * x_{(\lambda_1)} = -(a_{w(\lambda_1)} + b_{bw(\lambda_1)} * x_{(\lambda_1)}) \dots\dots\dots 4.31a$$

$$\begin{aligned}
 a_{ph(0.44)}(S_f a_{pico(\lambda_2)} + (1 - S_f) a_{micro(\lambda_2)}) + \\
 a_{dg(0.44)} \exp(-s(\lambda_2 - 0.44)) + b_{b,spm(0.4)} \left(\frac{0.4}{\lambda_2}\right)^y * x_{(\lambda_2)} = \\
 - (a_{w(\lambda_2)} + b_{bw(\lambda_2)} * x_{(\lambda_2)}) \quad \dots\dots 4.31b
 \end{aligned}$$

$$\begin{aligned}
 a_{ph(0.44)}(S_f a_{pico(\lambda_3)} + (1 - S_f) a_{micro(\lambda_3)}) + \\
 a_{dg(0.44)} \exp(-s(\lambda_3 - 0.44)) + b_{b,spm(0.4)} \left(\frac{0.4}{\lambda_3}\right)^y * x_{(\lambda_3)} = \\
 - (a_{w(\lambda_3)} + b_{bw(\lambda_3)} * x_{(\lambda_3)}) \quad \dots\dots 4.31c
 \end{aligned}$$

The above equations are written in matrix form in order to solve the unknowns as:

$$\begin{bmatrix} a_{ph(0.44)} \\ a_{dg(0.44)} \\ b_{b,spm(0.4)} \end{bmatrix} \begin{bmatrix} S_f a_{pico(\lambda_1)} + (1 - S_f) a_{micro(\lambda_1)} & \exp(-s(\lambda_1 - 0.44)) & \left(\frac{0.4}{\lambda_1}\right)^y * x_{(\lambda_1)} \\ S_f a_{pico(\lambda_2)} + (1 - S_f) a_{micro(\lambda_2)} & \exp(-s(\lambda_2 - 0.44)) & \left(\frac{0.4}{\lambda_2}\right)^y * x_{(\lambda_2)} \\ S_f a_{pico(\lambda_3)} + (1 - S_f) a_{micro(\lambda_3)} & \exp(-s(\lambda_3 - 0.44)) & \left(\frac{0.4}{\lambda_3}\right)^y * x_{(\lambda_3)} \end{bmatrix} = \begin{bmatrix} - (b_{bw(\lambda_1)} * x_{(\lambda_1)} + a_{w(\lambda_1)}) \\ - (b_{bw(\lambda_2)} * x_{(\lambda_2)} + a_{w(\lambda_2)}) \\ - (b_{bw(\lambda_3)} * x_{(\lambda_3)} + a_{w(\lambda_3)}) \end{bmatrix}$$

To solve the above mentioned equations by inverting remote sensing reflectance to derive IOPs, matrix inversion model of Wang et al. (2005) has been adapted. The model was run by using the full and reduced Ramses data. Besides, to derive the water quality variables from Landsat-8, the reflectance from its first five OLI bands their wavelengths centred at as mentioned in Table 4 have been used. Therefore, the model was run by considering more wavelengths (number of equations) than unknowns. Reference is made to Appendix 2 where the flow chart of water quality retrieval is shown. The general flow chart is given in Figure 4.

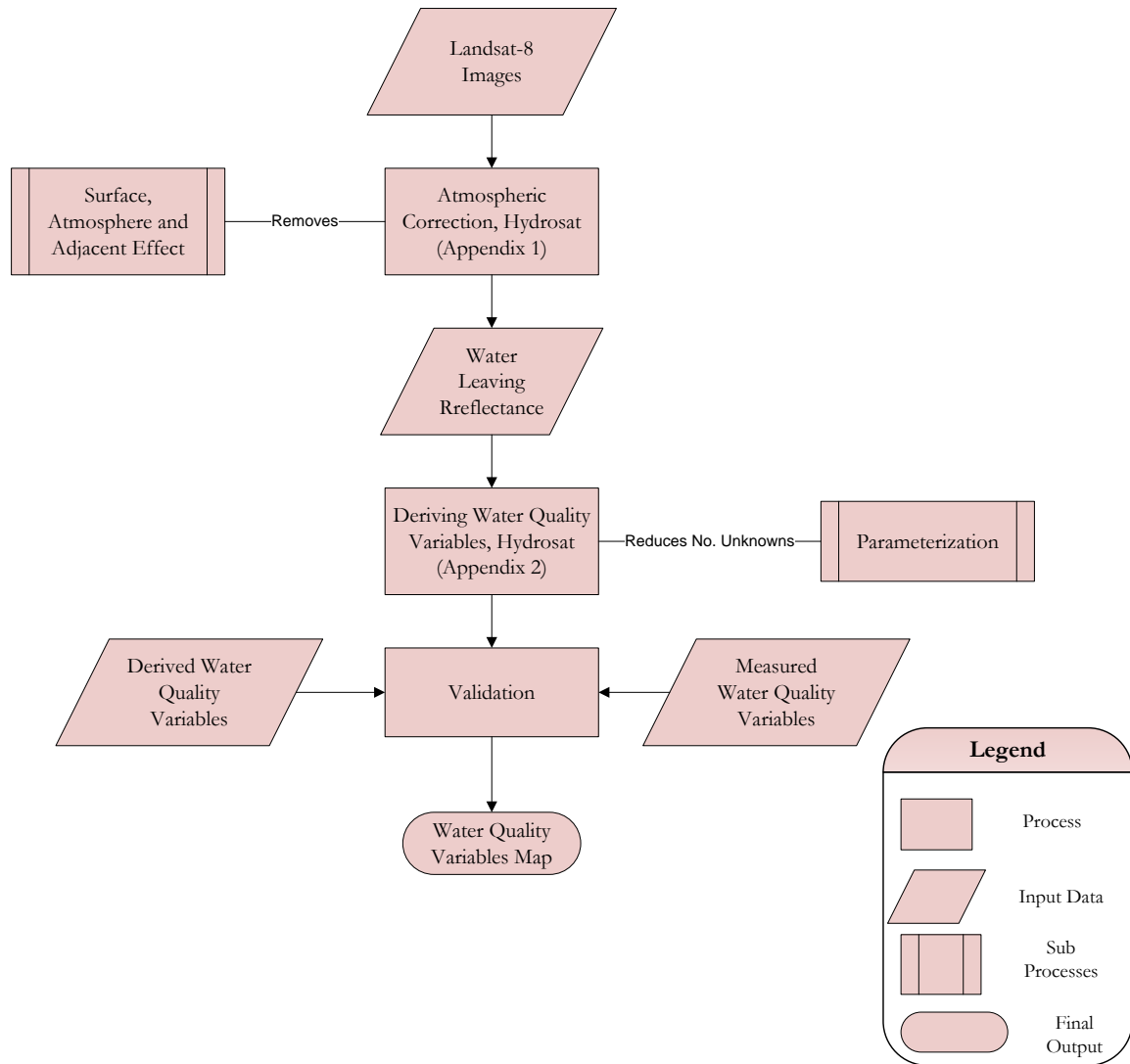


Figure 4 General flow chart of water quality retrieval method

4.8. Error Analysis

Error analysis provides information due to uncertainties in data measurement, model parameterization and approximation. The root mean square error (RMSE), relative root mean square error (rRMSE) and the standard deviation (σ) between in-situ measured and atmospheric corrected remote sensing reflectance, mean absolute error (MAE) between the measured and derived SPM concentration, have been analysed to estimate the error. Also the coefficient of determination (R-squared) value has been analysed to have information about the goodness of fit of a model used and to know how well the regression line approximates the real data points. The coefficient of determination gives an idea of how many data points lie within the results of the line formed by regression equation. Its value range is between 0 and 1. The coefficient of determination is calculated as follows.

For the measured (observed) water quality values of X_i the mean is calculated as:

$$\bar{X} = \frac{1}{n} \sum_{i=1}^n X_i \dots\dots\dots 4.32$$

Where n is the number of measurements.

The variability of the measurement can be computed through the total sum of squares (SS_{total}), the regression sum of the squares (SS_{reg}) and residual sum of squares (SS_{res}) as:

$$SS_{total} = \sum_i (X_i - \bar{X})^2 \dots\dots\dots 4.33$$

$$SS_{reg} = \sum_i (Y_i - \bar{X})^2 \dots\dots\dots 4.34$$

$$SS_{res} = \sum_i (X_i - Y_i)^2 \dots\dots\dots 4.35$$

Where Y_i is estimated water quality variables. By combing the above equations the coefficient of determination can be computes as:

$$R^2 = 1 - \frac{SS_{res}}{SS_{total}} \dots\dots\dots 4.36$$

The standard deviation is a measure of how the variables are spread out and it is the square root of the average of the squared difference from the mean and is computed as:

$$\sigma = \sqrt{\frac{1}{N} \sum_{i=1}^N (x_i - \mu_i)^2} \dots\dots\dots 4.37$$

Where x is the water quality variable and μ is the mean of the water quality variables.

The RMSE is the measure of the average magnitude of error and calculated as:

$$RMSE = \sqrt{\frac{1}{N} \sum_{i=1}^N (Rrs_{Image,i} - Rrs_{field,i})^2} \dots\dots\dots 4.38$$

The rRMSE can be computed as:

$$rRMSE = \sqrt{\frac{1}{N} \sum_{i=1}^N \left(\frac{Rrs_{Image,i} - Rrs_{field,i}}{Rrs_{field,i}} \right)^2} \dots\dots\dots 4.39$$

The closeness of the derived and measured concentration of SPM has been evaluated by quantifying the MAE. The MAE measures the average magnitude of errors in estimation without considering the direction of the error and all the individual variations are weighted equally in average. The MAE is calculated as;

$$MAE = \frac{1}{N} \sum_{i=1}^N |SPM_{derived,i} - SPM_{measured,i}| \dots\dots\dots 4.40$$

The MAE is always less or equal to the RMSE. If they are equal then all the errors are in the same magnitude. The range of the value of MAE and RMSE can be from 0 to ∞ . MAE and RMSE are based on the absolute error whereas the rRMSE is based on the relative error rather than the absolute. The value of rRMSE ranges from 0 to infinity. The errors in most of the remote sensing based water quality retrieval processes has been analysed using the above mentioned equations (IOCCG, 2006). Moreover the 95% confidence of interval for the derived values of SPM concentration (Y) from the measured values of SPM concentration (X) can be estimated as:

$$Y \pm t_{crit} s.e. \dots\dots\dots 4.41$$

Where *s.e.* is standard error of the regression line and is calculated as:

$$s.e. = S_{yx} \sqrt{\frac{1}{n} + \frac{(X_i - \bar{X})^2}{SS_x}} \dots\dots\dots 4.42$$

Where SS_x sum of squares of deviations and is calculated using DEVSQ function in excel as:

$$SS_x = \sum_i^n (X_i - \bar{X})^2 \dots\dots\dots 4.43$$

In general the 95% confidence level for the regression line is defined as:

$$Y \pm t(\alpha, df) S_{yx} \sqrt{\frac{1}{n} + \frac{(X_i - \bar{X})^2}{\sum_{i=1}^n (X_i - \bar{X})^2}} \dots\dots\dots 4.44$$

Where S_{yx} is the standard error of the estimated Y-value for each X in the regression and it is a measure of error in the estimation of Y for and individual X. It can be computed from the excel function STEYX.

Where t is the critical t statistic and can be computed from TINV function in excel. α is the probability and df is the degree of freedom.

5. RESULTS AND DISCUSSIONS

5.1. Results from In-situ Measurement and In-situ Data Analysis

5.1.1. Water Quality Variables from the Field Measurement

The concentration of CDOM and SPM, the absorption of chlorophyll-a, and the turbidity of water were measured in the laboratory from the collected water samples. The minimum CDOM concentration (between the range from 3 to 7 $\mu\text{g/l}$) was measured on the first two sampling days on 9th of September near Gumara river inlet area and on 10th of September near Gelda river (seasonal river in the southeast of the lake) inlet area. The relative maximum (from 9 to 13.5 μm) was measured at distance from the river on the other days of measurements (refer Figure 1 and Figure 2 for the locations of rivers and field measurements). The overall measured concentration of CDOM in the lake is low. According to the study of Zhang et al. (2007) higher concentrations of CDOM in a lake are from the decomposition of submerged aquatic vegetation (for macrophyte dominated lakes) and from riverine inflow. Moreover, as described by Sasaki et al. (2005) the breakdown product of phytoplankton due to microbial activity during the period of a strong increase in phytoplankton abundance contributes for the increases of CDOM concentration in water. Even though the above mentioned contributors for the increases of CDOM concentration were not measured in Lake Tana, for overall measured low concentration of CDOM their low existence might be the reason. In addition, since Lake Tana is characterized by low nutrient concentration (Vijverberg et al., 2009; Wondie et al., 2007) and less abundance of chlorophyll-a (Wondie et al., 2007), the low concentration of CDOM in the lake might arise from this reason. From the laboratory measurement and the field observation it has been seen that the chlorophyll-a concentration was zero for almost all the measured points and for few points (6 points) the measurement returns positive values. The maximum SPM concentration was at the mouth of Gumara river inlet and started decreasing away from the river inlet. The turbidity followed the pattern of SPM concentration and they were linearly related with R^2 equals 0.85, and slope and intercept of 0.738 and 20.5 respectively. The measured water quality variables covered the wide range within the measured distance (40km). The collected data within this distance showed the variability of the water quality variables distribution in a wide range within the lake. However, the field measurements were taken place in five different days within in one month; therefore, the variability was not only due to the space but also in time. The maximum, mean, minimum and standard deviation values of the measured SPM, CDOM, turbidity and Chl-a have been given in Table 5.

Table 5 Water Quality Variables Measured in the Field

Water Quality Variables	No. Samples	Maximum	Mean	Minimum	Standard Deviation
SPM (mg/l)	79	310	67.34	15	40.8
CDOM ($\mu\text{g/l}$)	79	13.45	7.6	3.4	2.97
Turbidity (NTU)	79	283	70.2	45.7	32.77
Chl-a absorption (440) [m^{-1}]	79	0.0087	0.0006	0	0.0021

5.1.2. Downwelling Irradiance and Upwelling Radiance from the Field Measurement

The maximum and the minimum downwelling irradiance measured in the field are 1479.44 and 6.986 $\text{W}\cdot\text{m}^{-2}\cdot\text{nm}^{-1}$ respectively with the mean 664.16 $\text{W}\cdot\text{m}^{-2}\cdot\text{nm}^{-1}$ and standard deviation of 443.724 $\text{W}\cdot\text{m}^{-2}\cdot\text{nm}^{-1}$. The large difference in magnitude of downwelling irradiance between the minimum and the maximum values shows that there was a variation in weather condition between the days at which the measurements were taken. Even the value of irradiance can vary highly in fraction of seconds if the cloud passes in front of the sun (Mobley, 2004). The maximum, mean, minimum and standard deviation of upwelling radiances are 73.67, 16.016, 0.077 and 14.456 $\text{W}\cdot\text{m}^{-2}\cdot\text{sr}^{-1}\cdot\text{nm}^{-1}$, respectively. The upwelling radiance measured just above the water depends on the constituents of water body and the directional structure of the ambient light field (Mobley, 2004). Therefore, its change in magnitude shows the spatial and temporal variability of the water constituents and the spatial, temporal and directional structure of light field. The downwelling irradiance and upwelling radiance measured in the field have been shown in Figure 5. The radiometric values presented in Figure 5 are within spectral range between 319 to 951nm in 1nm interval.

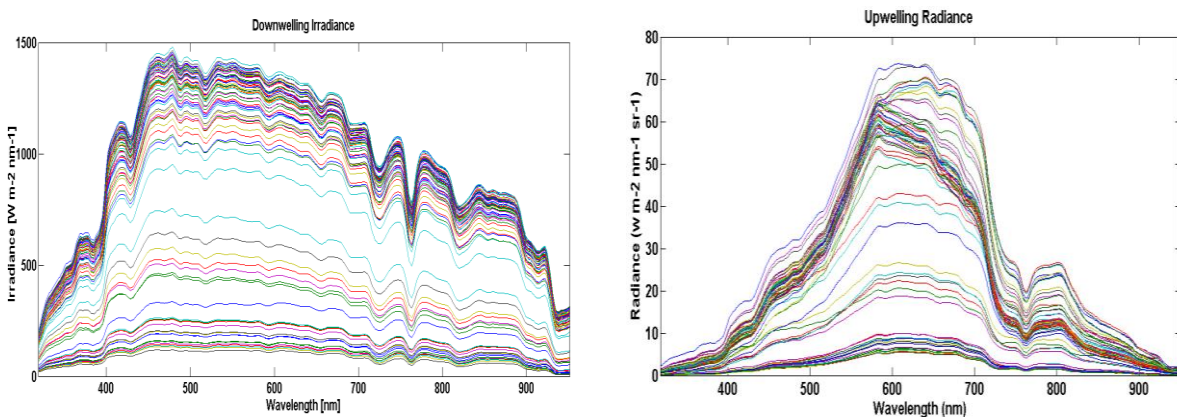


Figure 5 Downwelling Irradiance (left) and Upwelling Radiance (right)

5.1.3. Remote Sensing Water Leaving Reflectance from Ramses Data

The remote sensing water leaving reflectance from the field measurement was dominated by the absorption from water molecule, absorption from detritus and gelbstoff, backscattering from water molecule and backscattering from particulate matter. It has been computed from the field measured upwelling radiance and downwelling irradiance as discussed in section 4.5.1. The output from the computation has been shown in Figure 6 and the result is discussed hereafter. The reflectance in the first part of the spectrum (UV and blue region) is low and starts increasing to approximately 700nm. The maximum reflectance occurs around the region between 560 to 700nm. After 700nm the reflectance starts decreasing up to 780nm. From 780 to 820nm it increases again and after 820 starts decreasing. The variation of the magnitude of the remote sensing water leaving reflectance in each wavelength indicates the specific properties of each optically significant constituents and their significant effect on the light field as a function of wavelengths. Among optically significant constituents the water quality constituents, derived from remote sensing water leaving reflectance, affect the propagation of light in the water column and their spectral responses have been discussed in the next sections. The maximum remote sensing reflectance obtained from the field measurement was 0.065 with mean, minimum and standard deviation of 0.021, 0.00041 and 0.0152 sr^{-1} , respectively.

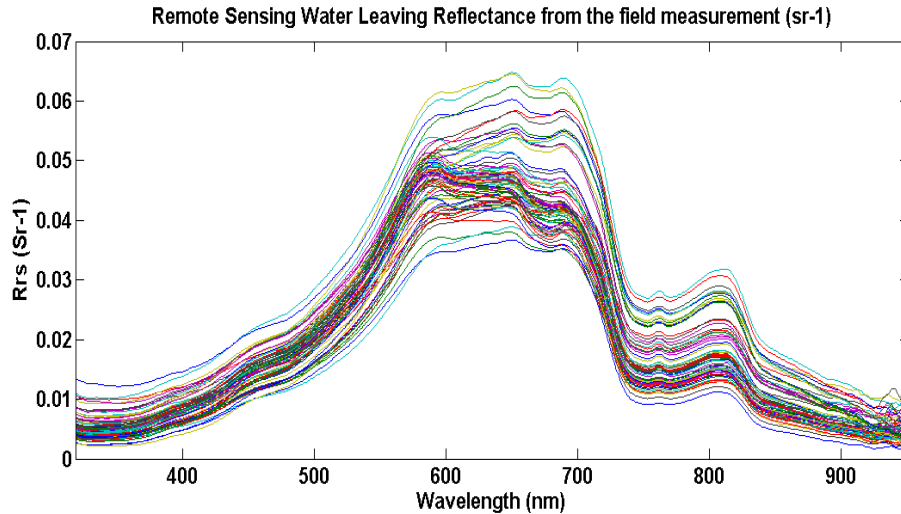


Figure 6 Remote Sensing Water Leaving Reflectance

5.1.4. Downwelling attenuation coefficients

The combined absorption and scattering properties of all constituents in the water column including the water itself cause decrease in the intensity of light as it travels through the water column (called light attenuation). In coastal and lake waters attenuation coefficient is higher than from open oceanic waters (Wang et al., 2008). The average downwelling attenuation coefficients at the depth 50cm below the water surface were calculated for the entire field measured points and they have been shown in Figure 7. From this figure it has been observed that the attenuation coefficient tends to decrease with wavelength increase in the spectral range from 410 to 700nm, while in the range between 700 to 750nm it tends to increase. For the wavelength of 750 to 820nm it tends to decrease and after 820 to 950nm it tends to increase again. The maximum K_d has been occurred around wavelength between 410 to 440nm and the minimum K_d has been occurred around 700nm wavelength. Among all samples, the maximum, mean and minimum values of attenuation coefficient are 23.6 , 8.4 , and $2.4 m^{-1}$ respectively with the standard deviation of $4.2m^{-1}$. As shown in (Austin & Petzold, 1986; Lee et al., 2005) it is possible to build a relation between $K_d(\lambda)$ and $K_d(490)$. For Lake Tana the analyzed mean value of $K_d(490)$ was $10.285 m^{-1}$ within the range $6.288 - 21.152 m^{-1}$. The results of $K_d(\lambda)$ fairly showed that the UV and blue light are highly attenuated by the water constituents, most likely due to SPM and CDOM.

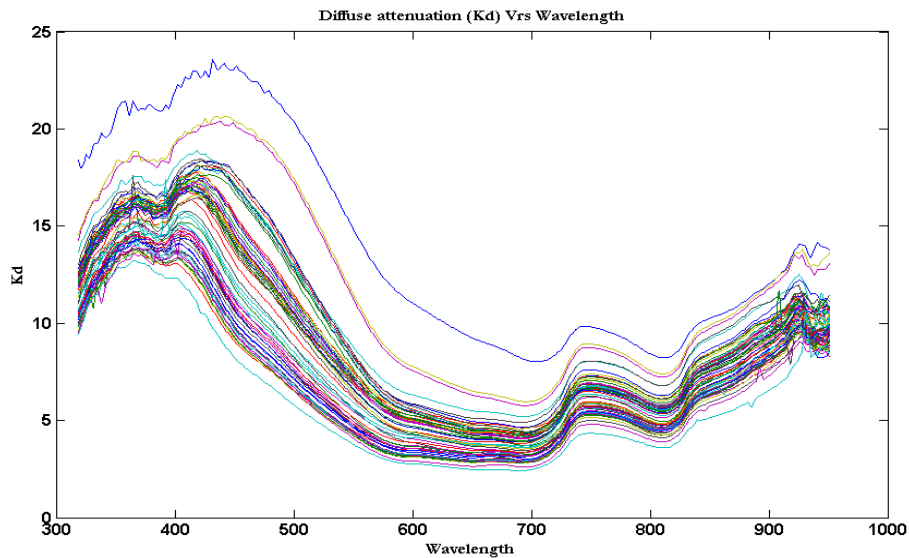


Figure 7 Downwelling Attenuation Coefficient

5.1.5. IOPs Retrieved from In Situ Measurement (Hydro-Optical Model Inversion)

5.1.5.1. Absorption coefficient of Phytoplankton for the full and reduced Ramses Data

For the retrieval of phytoplankton coefficient, the full Ramses data (from 400 to 700nm) was used. The retrieved phytoplankton absorption coefficient showed two peaks at the blue (440nm) and at the red (676nm). These peaks have been clearly shown in Figure 8. Whereas, for the reduced Ramses data set we missed these peaks mainly at the red region since its absorption was analysed within the range of 443 to 654.5nm. The field measurement points' bad spectra which returned the negative values of the phytoplankton absorption coefficient were removed from the results.

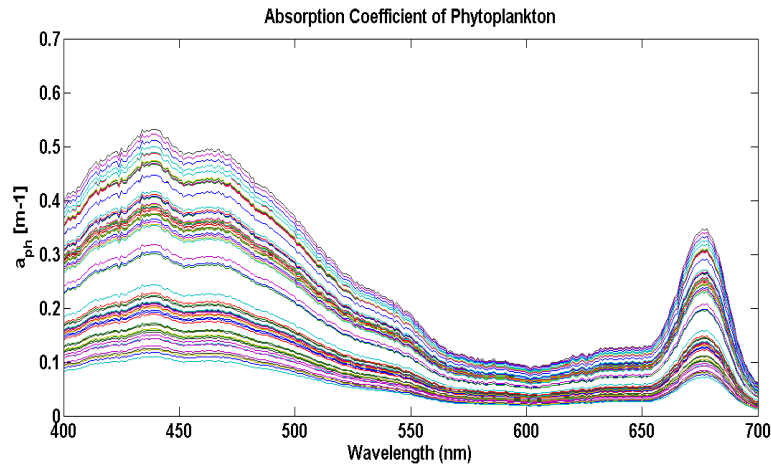


Figure 8 Absorption Coefficient of Phytoplankton from Ramses data

The maximum, mean, minimum and standard deviation values of $a_{ph}(440)$ and $a_{ph}(676)$ from the full Ramses data were analysed and tabulated in Table 6.

Table 6 Absorption Coefficient of Phytoplankton from Ramses data

	Maximum (m^{-1})	Mean (m^{-1})	Minimum (m^{-1})	Standard deviation (m^{-1})
$a_{ph}(440)$	0.655	0.301	0.065	0.139
$a_{ph}(676)$	0.426	0.196	0.042	0.091

However, these phytoplankton absorption values returned by the model inversion are unrealistic and contradicted with the field measurement and the observed actual water quality status of the lake. Therefore the model adopted in this study is not good for the retrieval of the actual phytoplankton absorption in the Lake Tana. For this study the field measurements were carried out in the last month of winter period (rainy season) and it was observed that the Lake Tana was free of algal particles. Relative to the other water constituents which contribute to light attenuation, the spectral response from phytoplankton absorption was low. Moreover it has been studied by different scholars (Matsuoka et al., 2011; Sasaki et al., 2005; Zhang et al., 2007) that in winter the significant decrease in phytoplankton absorption has been observed. One of the reasons to decrease the phytoplankton absorption in winter is that the high absorption by non-algal particles in the blue light and the rapid decrease of the blue light in the water column. The spectral response measured (R_{rs} , Figure 6) showed that the response from the phytoplankton in its peak absorption wavelengths was not as such significant. The correlations between model derived IOPs by considering phytoplankton absorption with their respective concentrations have been evaluated and the resulting relationships between IOPs and concentrations were bad and unrealistic. The statistics between the derived absorption of detritus and gelbstoff with measured CDOM and SPM

concentrations as well as the derived backscattering coefficient of SPM with measured SPM concentration (by considering the phytoplankton absorption) are presented in Table 7.

Table 7 The relation between the derived IOPs by considering the phytoplankton absorption with their respective measured concentrations.

	Slope	Intercept	R-squared (R ²)
$a_{dg}(443)$ versus CDOM concentration	-0.0352	3.825	0.055
$a_{dg}(443)$ versus SPM concentration	0.0017	3.449	0.0206
$b_{bp}(443)$ versus SPM concentration	2×10^{-6}	0.483	2×10^{-7}

Therefore, due to the above discussed reasons the absorption of phytoplankton has been neglected from the model retrieval of water quality indicators. The derivation of IOPs in this study has been performed by neglecting the effect of phytoplankton. The derived IOPs by neglecting phytoplankton absorption have shown a strong linear relationship with the measurement (refer section 6).

5.1.5.2. Absorption Coefficient of Detritus and Gelbstoff ($a_{dg}(\lambda)$) from Ramses Full and Reduced Data

The absorption coefficient of the combined effect of detritus and CDOM was analysed by running the model for the full (319-950nm) and reduced Ramses data (refer Table 4). The absorption coefficient of the combined detritus and CDOM decreased exponentially with increasing wavelength over the 319 – 700nm range and approach zero after 700nm. Most of the ultraviolet and blue radiations were significantly attenuated by the combined effect of detritus and CDOM absorption. The mean combined detritus and CDOM absorption coefficient at 440nm ($a_{dg}(440)$) value was 13.65 m⁻¹ within the range of 8.03 – 18.40 m⁻¹. Since the reduced Ramses data has started from the wavelength 443nm, the absorption of detritus and gelbstoff at ultraviolet region (where the absorption of detritus and gelbstoff maximum) was not observed. Whereas, the absorption of detritus and gelbstoff from full Ramses data includes the absorption in ultraviolet region.

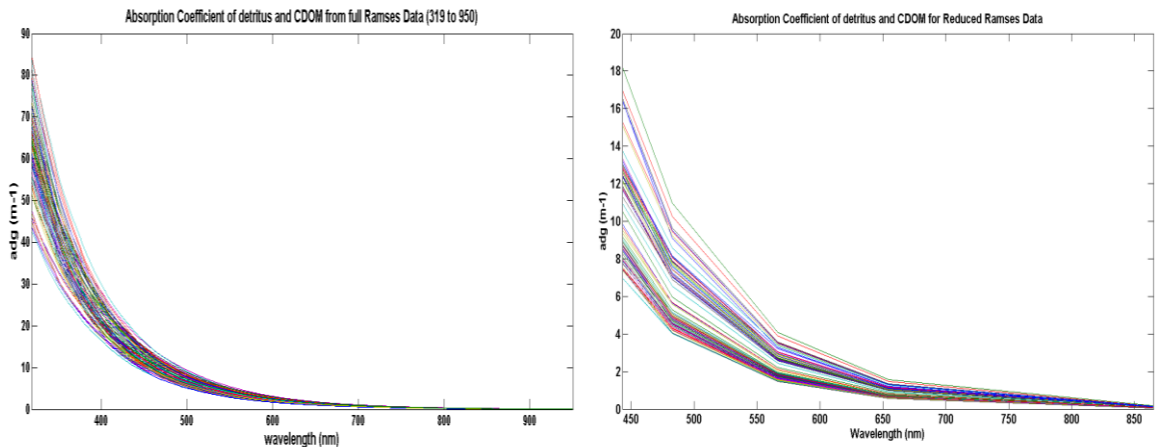


Figure 9 Absorption Coefficient of detritus and CDOM (the right figure shows the absorption coefficient of detritus and gelbstoff from full Ramses data (the wavelength started at 319 and ends at 950) and the left shows the absorption of detritus and gelbstoff from reduced Ramses data (the wavelength starts at 443nm and ends at 865nm).

5.1.5.3. Backscattering Coefficient of Particulate Matter

The backscattering coefficients of SPM derived from full and reduced Ramses data have been shown below in Figure 10. The backscatter coefficients increased exponentially as the wavelength decreases. The SPM concentrations measured at the mouth of Gumara river inlet were high and the corresponding

backscattering coefficients in this area were relatively higher than the others since the SPM concentration was significantly high. The variation of SPM concentration was observed within one month interval and Figure 10 shows the effect of the variation of SPM on incoming light. The SPM measured at the beginning and the end of the same month from the same area showed a significant difference. The SPM concentration measured at the beginning of the field measurement month (9th of September) at the Gumara river inlet is much higher than the measurement taken at the end of the month (26th September) of the same area. This shows the decrease of suspended sediment load from the river when the end of the rainy season approaches. The maximum, mean, minimum and standard deviation values of backscattering coefficient of SPM at wavelength of 440nm are 2.99, 1.125, 0.59 and 0.365m⁻¹ respectively. The backscattering coefficient of SPM from full Ramses data gives information about the attenuated light due to SPM concentration in the water column starting from ultraviolet region. Whereas, the backscattering coefficient from reduced Ramses data contain information of light attenuated by SPM concentration in water column starting from the blue region.

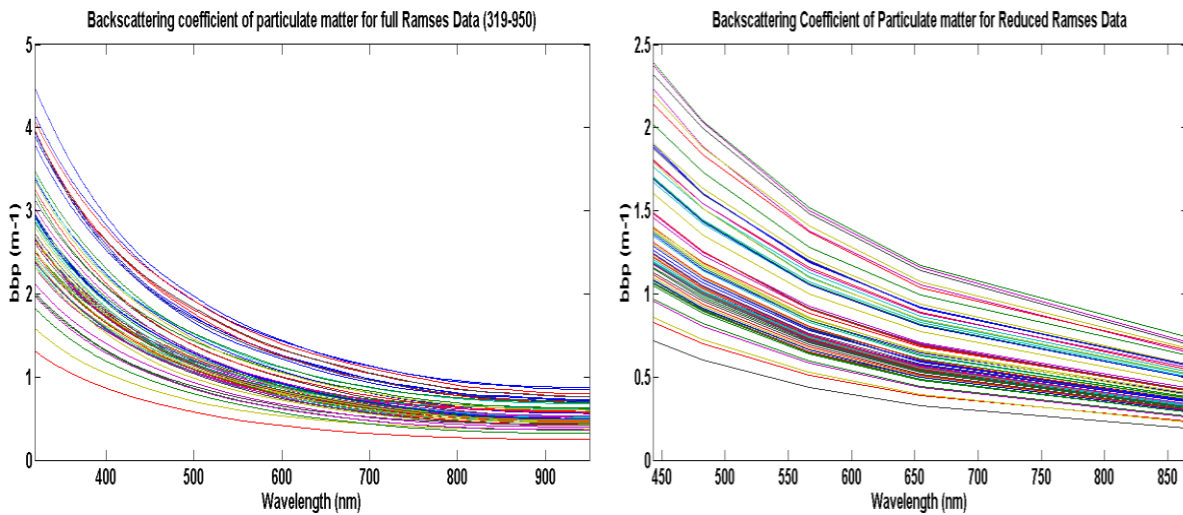


Figure 10 Backscattering Coefficient of SPM (the left is from full Ramses data and the right is from reduced Ramses data). The difference between the left and the right figure is that, the left starts from 319nm and ends at 950 and it is useful to study the UV light attenuation by SPM. However, the right figure starts from 443nm and ends at 865 and it only gives information about light attenuation by SPM starting from blue region.

5.2. Results from the Image Data

5.2.1. Atmospheric correction (From Hydrosat)

The Hydrosat atmospheric correction method was applied to the Landsat-8 image of September 26th 2013 after implementing the first order haze correction. The first order haze correction has been done by removing the resulting reflectance of cirrus band (band 9) from the top of atmosphere reflectance of each other bands. The Hydrosat atmospheric correction method was then applied on the first order haze corrected image matchup-data and the resulting values of averaged TOA, atmospheric corrected and in-situ measured reflectance have been shown in Figure 11. When it has been compared with other bands (Green, Red, and NIR) the atmospheric corrected reflectance in deep blue and blue region is much higher than from the in-situ water leaving reflectance. The atmospheric corrected and the in-situ reflectance data are well fit in green, red, and NIR bands than deep blue and blue bands. Therefore, the Hydrosat atmospheric correction method corrected well the bands from green to NIR.

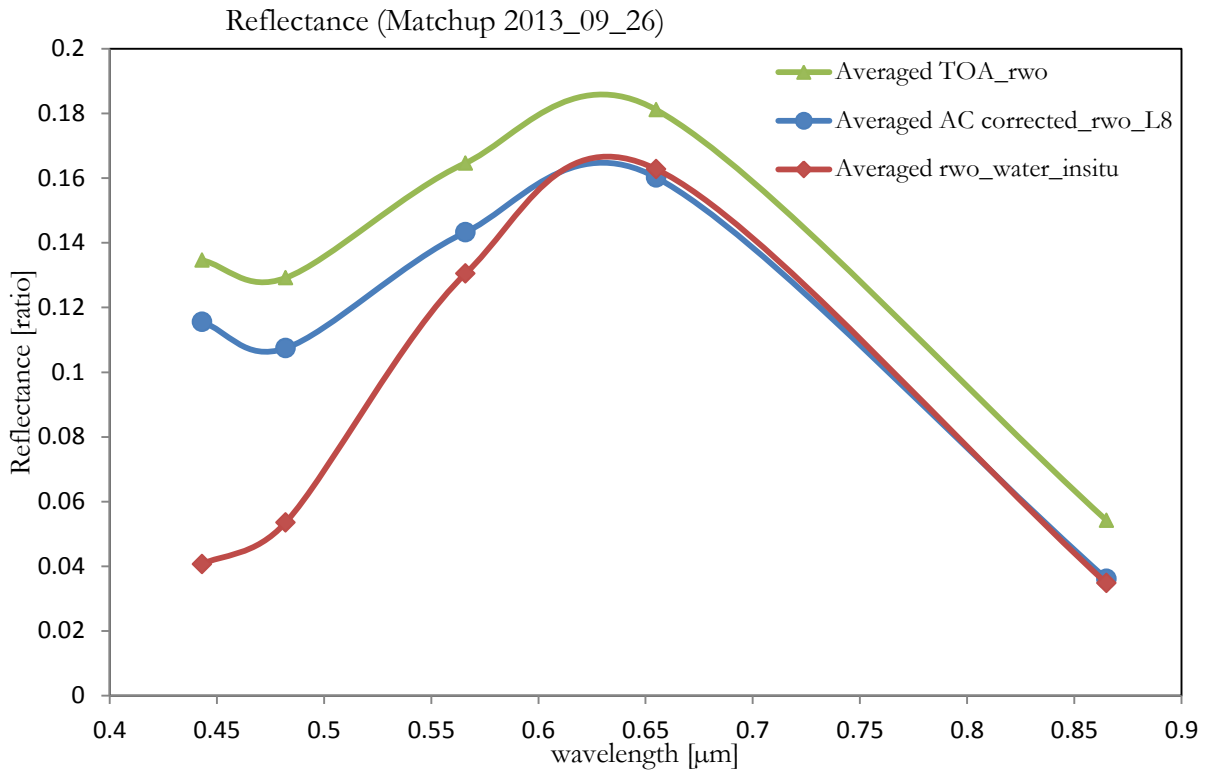


Figure 11 Comparison between TOA, Atmospheric Corrected and In-situ measured Reflectances (2013/09/26)

5.2.2. Verification of Atmospheric correction

The accuracy of Hydrosat atmospheric correction method was evaluated through the comparison between the derived atmospheric corrected water leaving reflectance from the image and the measured water leaving reflectance on the same day of satellite overpass. The computed slope, intercept, R² and RMSE between atmospheric corrected image reflectance of each band with the corresponding in-situ measured reflectance for the matchup data are presented in Table 8.

Table 8 Relation between Atmospheric Corrected and In-situ Measured Reflectance

Bands L-8	Wavelength (nm)	No. Samples	slope	intercept	R ²	RMSE [ratio]
Band 1	443	9	0.171	0.108	0.81	0.075118
Band 2	482	9	0.173	0.1	0.84	0.05701
Band 3	566	9	0.114	0.131	0.79	0.018434
Band 4	655	9	0.107	0.145	0.83	0.016246
Band 5	865	9	0.228	0.028	0.82	0.005548

The RMSEs between the reflectance obtained from the satellite after atmospheric correction and the in-situ measurement of each band of the matchup data were compared and shown in Figure 12. The RMSEs of bands from 3 -5 were small and showed a slight variation. Therefore, for these bands, the Hydrosat atmospheric correction method estimated the water leaving reflectance fairly and accurately.

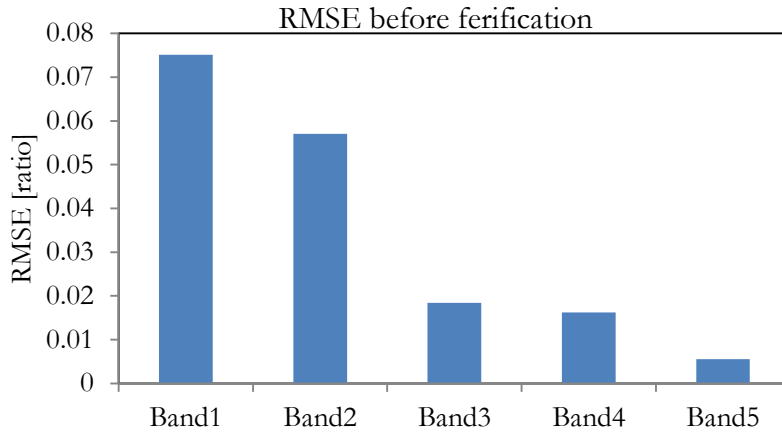


Figure 12 RMSE between field measured and atmospheric corrected reflectance

To correct for the atmosphere residual, the difference between the atmospheric corrected reflectance and the in-situ measured water leaving reflectance was computed and fitted as shown in Figure 13. From the fit curve equation, the delta value (δ) for each band has been computed. The obtained delta value of each band can be tuned into Hydrosat atmospheric correction method to obtain the atmospheric corrected reflectance for the entire image.

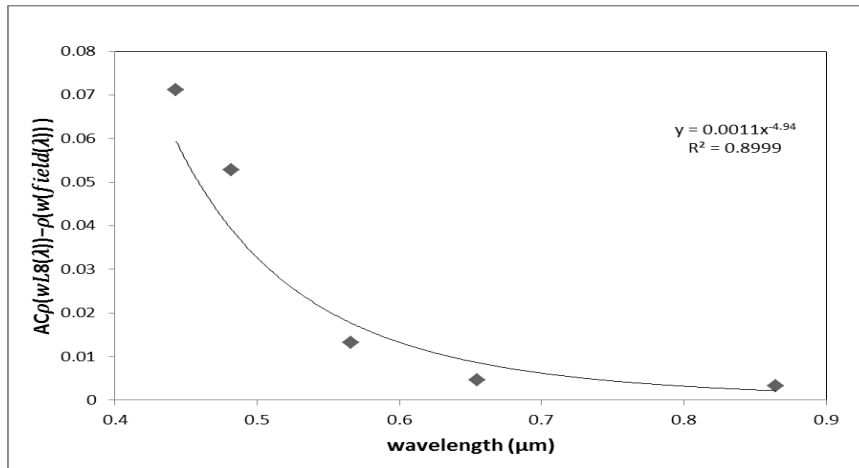


Figure 13 Difference between atmospheric corrected and field measured Rrs

The delta (δ) has been computed as;

$$\rho_{w_L8}(\lambda) - \rho_{w_field}(\lambda) = 0.0011 * \lambda^{-4.94}$$

$$\rho_{w_L8}(\lambda) = \rho_{TOA}(\lambda) - \epsilon_{(s,l)}^{\delta(\lambda)} * \rho_{a(l)}$$

$$\epsilon_{(s,l)}^{\delta(\lambda)} = \frac{(\rho_{TOA}(\lambda) - \rho_{w_field}(\lambda) - 0.0011 * \lambda^{-4.94})}{\rho_{a(l)}}$$

$$\delta(\lambda) = \frac{\log \left[\frac{(\rho_{TOA}(\lambda) - \rho_{w_field}(\lambda) - 0.0011 * \lambda^{-4.94})}{\rho_{a(l)}} \right]}{\log \epsilon(s, l)} \dots \dots \dots (5.1)$$

After implementing the new delta (δ) value from equation 5.1 in Hydrosat atmospheric correction equation (equation 4.18), the verified atmospheric corrected water leaving reflectance has been obtained. The verification has reduced the RMSE more in deep blue and blue region of the image. For the other regions of spectra (Green- NIR) there is no a significant different between the obtained atmospheric corrected reflectance from the original Hydrosat and the verified methods. Therefore, the delta (δ) from equation 5.1 can only be used for the blue to green region of the spectra. The comparison between the TOA, verified atmospheric corrected and in-situ water leaving reflectances has been show in Figure 14. The RMSEs (Figure 15) and relative root mean square error (rRMSE) before and after verification have been computed for each band, and presented in Table 9.

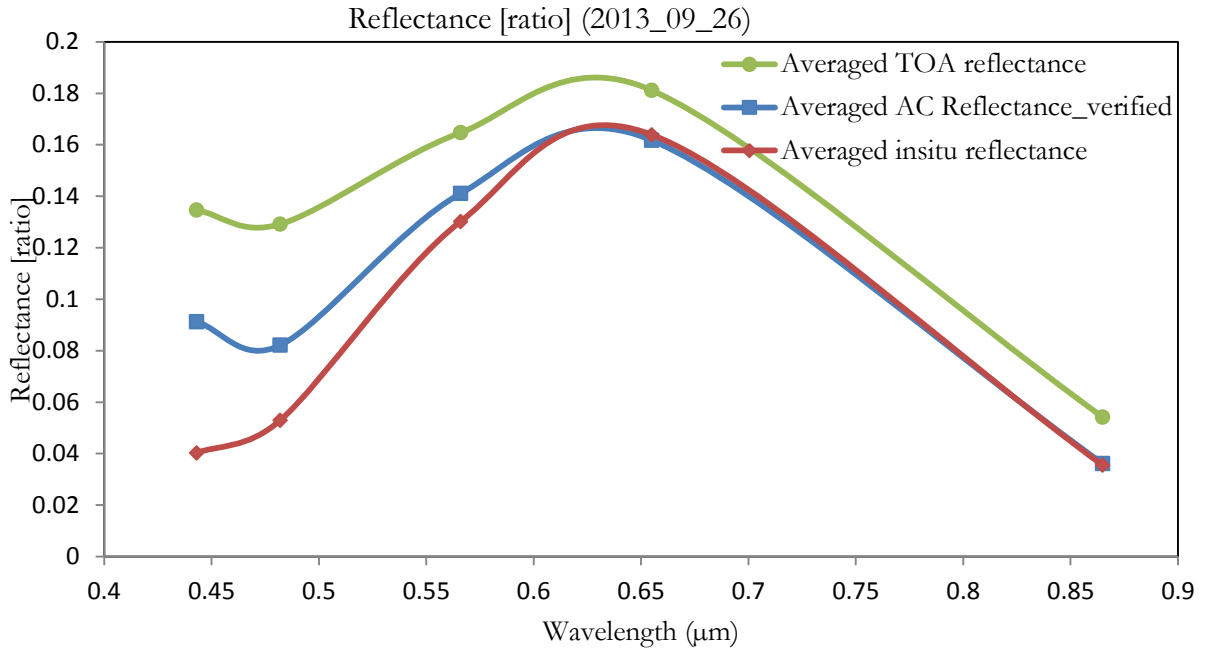


Figure 14 Comparison between averaged TOA, verified atmospheric corrected and in-situ watre leaving reflectances

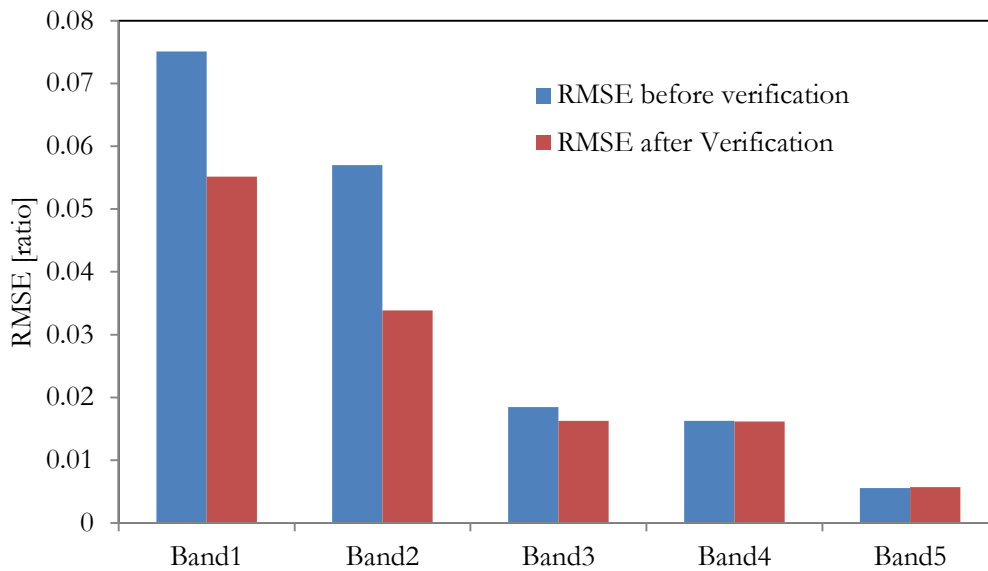


Figure 15 Comparison of RMSE before and after verification

Table 9 RMSE and rRMSE before and after verification

Bands	RMSE before [ratio]	RMSE after [ratio]	rRMSE before [%]	rRMSE after [%]	Difference of rRMSE [%]
Band1	0.075118	0.055153	201.7	149.433	52.267
Band2	0.05701	0.03386	113.8	68.923	44.877
Band3	0.018434	0.016279	15.04	13.284	1.756
Band4	0.016246	0.016169	10.05	10.011	0.039
Band5	0.005548	0.005688	17.88	18.098	-0.218

5.3. IOPs Derived from Landsat-8 image

After verification of the Hydrosat atmospheric correction method the IOPs have been derived from the verified water leaving reflectance of the matchup data first and then from the entire image data. As shown in Figure 14, in the blue region the water leaving reflectance from the Ramses is lower than from the image. Since the derived IOPs depend on the water leaving reflectance, the absorption coefficient from the image was less than from the Ramses whereas the backscattering coefficient from the image was greater than from the Ramses from blue to green region of spectra. From green to NIR region of spectra the IOPs from image and Ramses were approximately equal. The derived IOPs from the image have shown a strong linear relation with measured SPM concentration. The IOPs of the lake derived for the entire lake from the images have been discussed and presented in section 7.

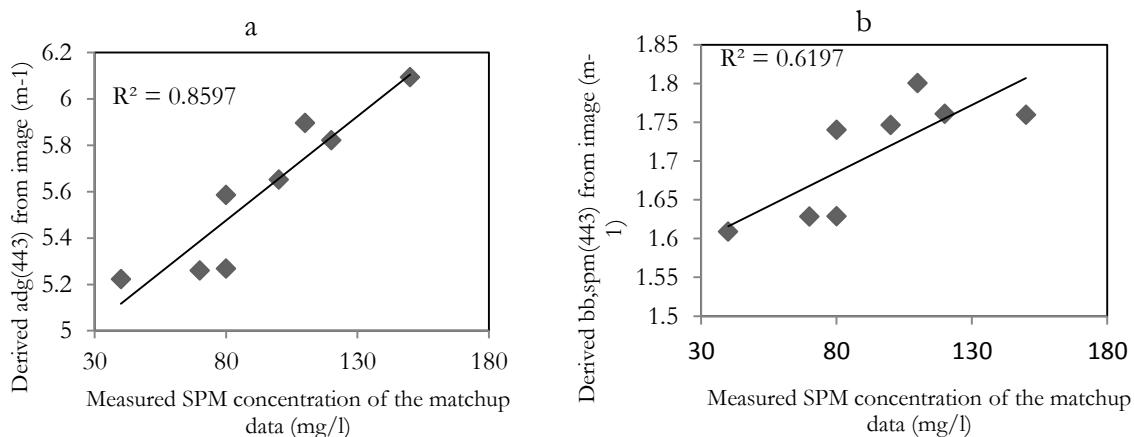


Figure 16 The IOPs derived from the matchup data of image (26 September 2013). (a) derived absorption coefficient of detritus and gelbstoff at 443nm versus measured SPM concentration and (b) the derived backscattering coefficient of SPM at 443nm versus measured SPM concentration

6. CALIBRATION, VALIDATION AND UNCERTAINTY

6.1. Calibration and Validation of IOPs

The IOPs of the constituents can be linearly related to their concentrations through the specific inherent optical properties (SIOPs). The specific inherent optical property (SIOP) of SPM was computed using GeoCalVal model (Salama et al., 2012a). The backscattering coefficient of SPM at 443nm derived from Ramses data and the measured SPM concentration data have been randomly divided into Calibration (Cal) and Validation (Val) data sets. The Cal data set was used to derive the specific inherent optical property of SPM at 443nm and the Val data set was used to check the validity of the model to derive IOPs. The probability distribution of the model coefficients and the associated uncertainties are shown in Figure 17.

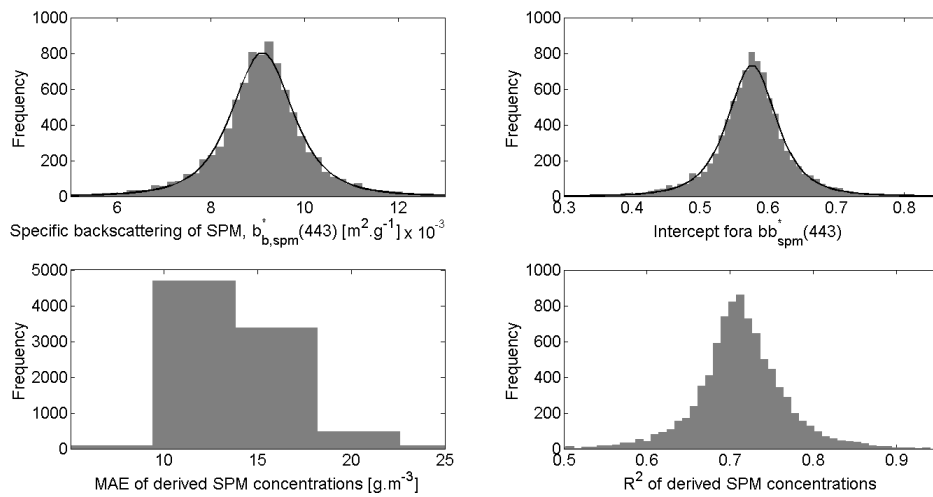


Figure 17 SIOPs and associated uncertainties

The mean R-squared, slope (SIOP), intercept and mean absolute error (MAE) computed from the model have been presented in Table 10.

Table 10 Calibration and Validation outputs

	R square (R ²)	Slope (b _{b,spm} [*] (443))	Intercept	Mean absolute Error (MAE)
b _{b,spm} (443)	0.72	0.0091 (m ² /g)	0.5766 (m ⁻¹)	13.57 (g/m ³)

In another hand the correlation between derived absorption coefficient of detritus and gelbstoff was analysed and the derived absorption coefficient at 443nm (a_{dg(443)}) and measured CDOM concentration seems well correlated. However, the decrease in absorption coefficient with an increase of a concentration was deviated from the reality and it didn't obey the Lambert Beer law (linear relationship between absorbance and concentration of absorbing constituent). Therefore the measured concentrations of CDOM were divided into two data sets based on the range of the measurement (Figure 18(a)) and then the correlation between the derived IOP of detritus and gelbstoff with measured CDOM concentration was evaluated again. As shown in Figure 18(b and c) below, the measured CDOM and the derived IOP of detritus and gelbstoff of the two data sets are poorly related. Comparison of derived IOP and measured CDOM concentration shows large deviations. Therefore, the absorption coefficient of detritus and gelbstoff was mainly governed by the detritus.

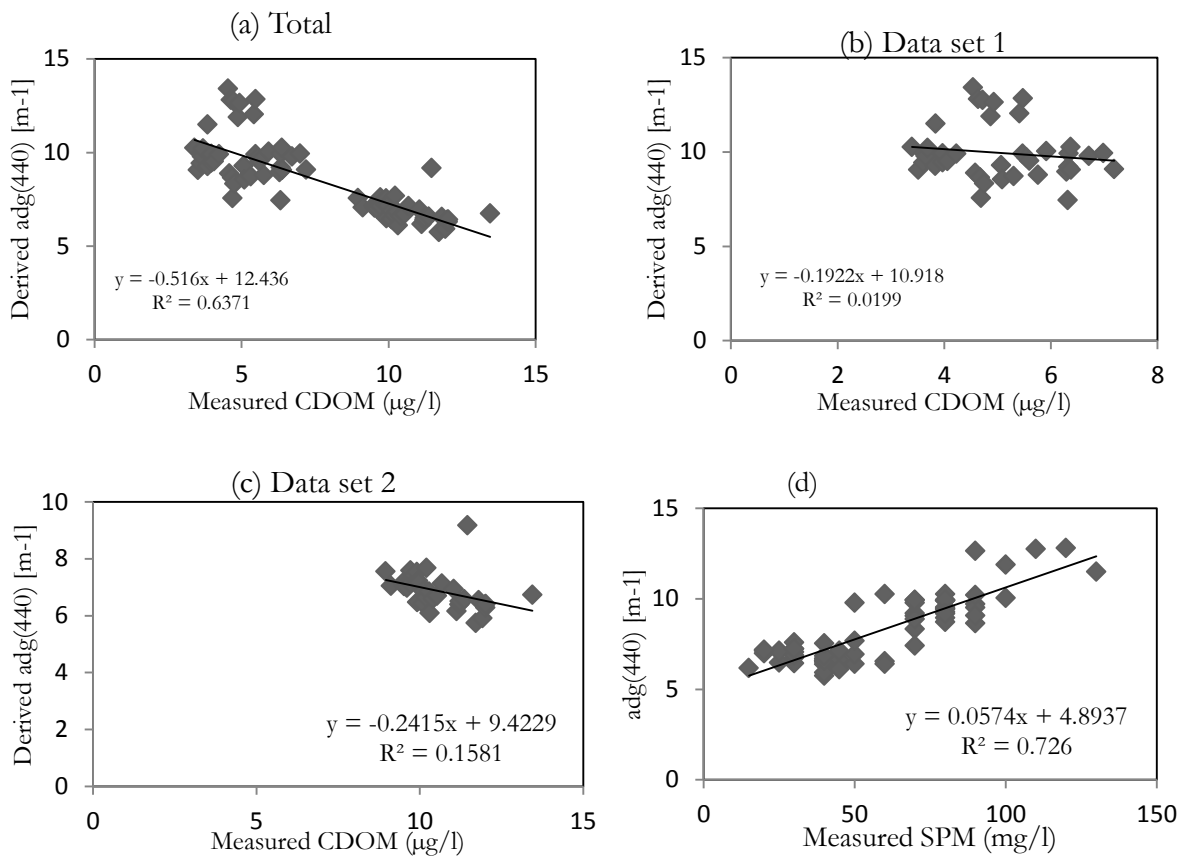


Figure 18 The relation between derived absorption coefficient of detritus and gelbstoff with measured CDOM (a-c) and SPM concentrations (d)

6.2. Validation of the Water Quality Variables

The concentrations of water constituents can be retrieved from the IOPs knowing the specific inherent optical properties of these constituents. So that the SPM concentrations were derived using the specific inherent optical properties obtained in section 6.1 by considering it as spatially constant. A few values with the bad spectra weren't considered for the derivation of model SPM concentration. The concentration of SPM derived versus measured has been shown in

Figure 19, and the measured and the derived SPM concentrations were correlated with R^2 value of greater than 0.7. Therefore, there is a linear relationship between derived and measured concentration of SPM. The 95% confidence interval for the linear regression line has been computed. The 95% confidence interval consists the space between the upper and the lower bound curves. This confidence interval for the estimated values of SPM concentration from measured SPM concentration shows that there is a 95% probability that the true linear regression line will lie within the calculated bound.

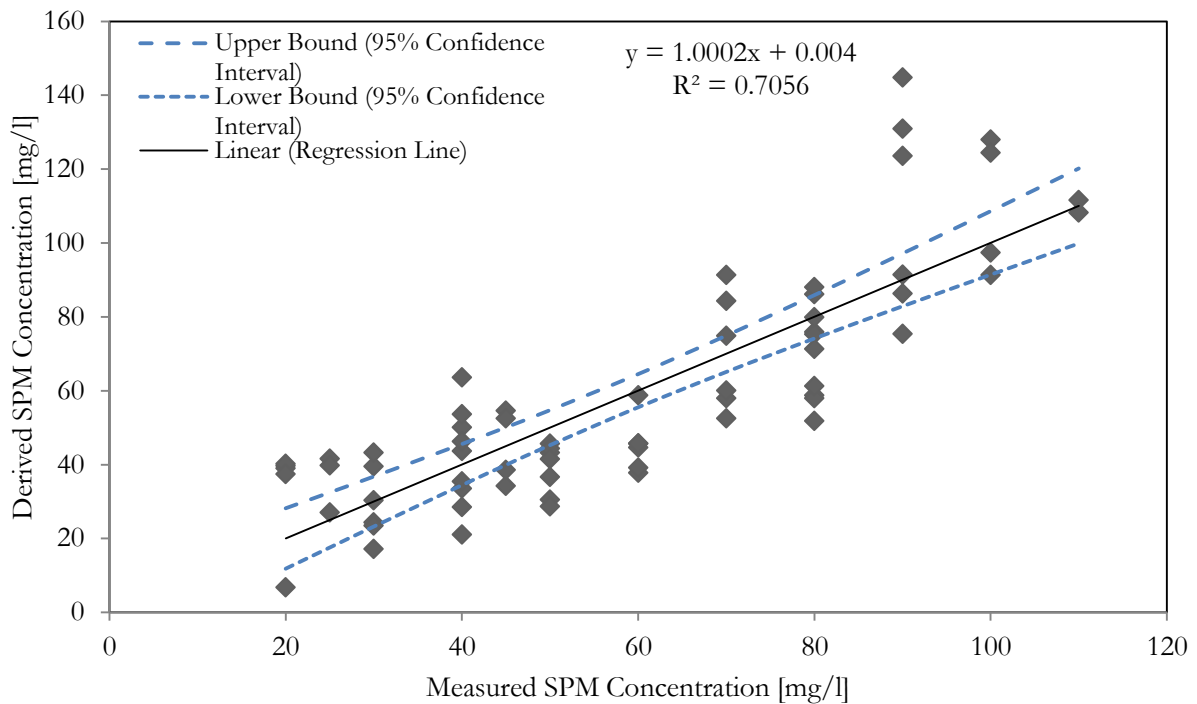


Figure 19 Derived SPM versus Measured SPM concentration

6.3. The Sources of Uncertainty

6.3.1. Data Uncertainty

The IOPs have been derived from the field measured and satellite image reflectance data by a hydro-optical model inversion as discussed in section 4.6 and 4.7. The adapted semi-analytical model for both data sets was the same. Whereas, analysis on IOPs derived from both data sets showed different values. The possible causes for the difference are discussed hereafter. In-situ data used for calibration and validation of the model contain significant levels of uncertainty caused by experimental and environmental factors (IOCCG, 2006). The various sources which introduce uncertainty in in-situ optical and water quality variables measurement are Calibration of measuring instruments, environmental condition confronted during in-situ measurement, the precision of measuring equipment, data processing, the water and the sky condition, etc. (Hooker & Maritorena, 2000). Spatial mismatch in scale between the match-up in-situ and the satellite data introduces another uncertainty. The match-up in-situ data represents an area of small scale (may be point) while the satellite observation represents larger spatial scale. Furthermore, the in-situ measurement often taken from discrete depth of water column, whereas the satellite observation represents weighted average (Zaneveld et al., 2005). The depth variation between the in-situ and the satellite measurements introduces uncertainty when they are related to each other. Uncertainties are also introduced from the pre-launch characterization of the sensor (IOCCG, 2006), atmospheric corrections, and observing wavelength range between in-situ and satellite radiometric measurement.

In general, the high turbidity characteristics of Lake Tana might lead to larger uncertainties (errors) since the uncertainty of IOPs and the turbidity of water are directly proportional (Ghezehegn, 2011; Salama et al., 2009). Uncertainties of IOPs derived from semi-analytical model inversion have been studied by many scholars (Salama et al., 2009; Salama & Stein, 2009b; Wang et al., 2005) and the source of error in the retrieval process were discussed.

6.3.2. Calibration Parameter Uncertainty of Landsat-8

Several calibration parameter updates have been implemented as part of the Landsat-8 data reprocessing since February 3, 2014. The early update is from the January 6, 2014 Calibration notices (<https://landsat.usgs.gov/index.php>). The reprocessing serves to improve product quality by modifying all calibration file updates since launch of the satellite; improve OLI reflectance conversion coefficients for the cirrus band; improve OLI radiance conversion coefficients for all bands; refine OLI detector linearization to decrease striping; correct a radiometric offset for both TIRS bands; a slight improvement to the geolocation of the TIRS data, and affect both the OLI and TIRS. After reprocessing the following improvement will be expected;

- Refining the OLI detector linearization correction coefficients for all spectral bands to decrease striping in imagery over dark uniform areas. However, the absolute radiometric accuracy is not significantly affected.
- Improving the OLI radiance conversion coefficients. On the reflectance values, mainly in the cirrus band, a slight improvement to the absolute accuracy will also be applied. To reduce striping in the cirrus band the updated in relative gains will be done, but the absolute radiometric accuracy will not be affected significantly.
- Implementing the new TIRS temperature offset that expected to remove an average error introduced by stray light coming from outside the TIRS field of view and will improve the data accuracy for typical growing season data (10° to 30° C) where the surrounding areas are similar in temperature.

The calibration parameters which have been implemented in this study were before the updates. So that the calibration parameters (the OLI radiance conversion coefficients) might introduced a slight error as much as a +2% (<https://landsat.usgs.gov/index.php>).

7. SPATIOTEMPORAL VARIABILITY OF WATER QUALITY INDICATORS IN LAKE TANA

For the spatiotemporal analysis four Landsat-8 images of the days 19 April 2013 (dry season), 24 July 2013 (the peak rainy season), 26 September 2013 (the end of rainy season) and 29 November 2013 (shortly after the end of rainy season) have been selected and evaluated. The temporal analysis was limited to only the start and end of rainy season of the year 2013 because images of Landsat-8 only are available starting from April 2013. For the general discussion of the IOPs, the water leaving reflectance (atmospheric corrected reflectance) of these selected images at band 1 (443nm) have been analysed and shown with natural colour composite of the images (Red=Band 4, Green=Band 3, Blue=Band 2) (Figure 20). Results of analysis of the effect of suspended particulate matter in water leaving colour, the water leaving reflectance of Band 5 (865nm) are shown in Figure 21. Maps of Lake Tana with water quality indicators are presented in Figure 22 and Figure 23. The maps presented in figures 20, 21, 22 and 23 were analysed and plotted using ENVI + IDL, Matlab and ArcGIS software.

The spatial variability of the lake's water quality variables was discussed by dividing the lake into six subareas based on the geographic location and the surrounding situations: such as Bahir Dar city (outflowing Blue Nile river, south), inlet of Gumara and Rib rivers (east), inlet of Gilgel Abay, Kilti, and Koga rivers (southwest), inlets of Dirma, Megech and Arno-Gurno rivers (north east), northwest and central part of the lake. The locations of the main inflowing rivers and outflowing river is in Figure 1.

The presence of suspended and dissolved matter in the waters increases both the scattering and absorption. Morel and Prieur (1977) studied that the increase in backscattering increases the water leaving reflectance more or less uniformly in every part of the spectrum. However, the increase in absorption decreases the water leaving reflectance. As discussed, the backscattering is from the water molecule and suspended particulate matter, and the absorption is from the water molecule, detritus, gelbstoff and chlorophyll-a pigments. Furthermore, in the infrared region the water absorbs predominantly and the scattering is due to suspended particulate matter (Salama et al., 2009) (Figure 21). From the available images of the year the IOPs distribution has been discussed focusing the four images of the lake.

7.1. Dry season (24 April 2013)

Before the start of rainy season the water leaving reflectance was low in the east, south and northeast parts of the lake. However, relatively higher reflectance has been observed in the northwest part of the lake. Therefore, in the northwest part of the lake the backscattering constituents were relatively greater than the other parts of the lake. Since main inflowing rivers (i.e. Gilgel Abay, Kelti, and Koga southwest, Gumara and Rib east, and Megech northeast) during this period were relatively clean and free of suspended particulate matter and diluted the particulate matter around the entrance, their corresponding areas of the lake appeared low of SPM (scattering constituents). On the contrary, the absorption of detritus and gelbstoff was higher in the rivers entry area and along the lakeshore. In the northwest central part of the lake the absorption effect of detritus and gelbstoff was relatively low. During this period the most likely absorbing constituent is gelbstoff (CDOM) rather than detritus. This is because the rivers can still transport soluble humic substances leached from the soil in the catchment area and the current of the lake water can decompose the plant matter and dissolve the humic substances in the soil along the shoreline. When compared with other periods, the concentration of SPM is lower and the low water leaving reflectance was observed during this period. Therefore, the lake mainly predominated by other absorbing constituents.

7.2. The peak rainy season (24 July 2013)

At peak rainy season the water leaving reflectance became higher than the dry season across the lake. This is due to the sediment load from the draining rivers and the agricultural drainage areas. In this main rainy season the heavy suspended sediment loads were carried by the six main rivers as well as small tributaries and caused the increase of turbidity of the lake mainly at the river inflow locations and along the lakeshore. Moreover, except the northeast part the lake, wet lands (floodplains) all around the lake (Vijverberg et al., 2009) were flooded and discharged into the lake during the rainy season and contributed to the SPM load to the lake. Since the increase of suspended sediment concentration reduced the underwater light intensity and the primary production in the lake, as the result absorbing constitute like chlorophyll-a pigment was diminished. Even though the other absorbing constituent diminished at this period, the absorption coefficient observed was high and followed the pattern of SPM. Both the scattering of SPM and absorption of detritus and gelbstoff have shown the same pattern. The IOPs are high across the lake but relatively low in the central part of the lake. The highest values of IOPs which were observed in the north-west part of the lake (Figure 22 and Figure 23) and presumably are caused by the heavy load of SPM from the seasonal river and the surrounding agricultural area. During peak rainy season the scattering and the absorption were predominated by SPM.

7.3. The end of rainy season (26 September 2013)

At the end of the rainy season the water into the lake is relatively clean and the suspended sediment loads were reduced. The northeast and east part of the lake appeared with low concentration of SPM. However, the overall maximum SPM concentration was observed at this time, and the sediment was shifted to the west side of the lake and the highest value was derived at the southwest central part of the lake (refer Figure 23). Relative to the outlet area of Gilgel Abay river, the outlet areas of Gumara, Rib and Megech appeared clear. The absorption of detritus and gelbstoff derived during this period is high across the lake (Figure 22). The absorption in the northwest, west and south part of the lake most likely predominated by detritus. The maximum absorption was retrieved in the northeast part of the lake and the effect of gelbstoff probably took a lead at this part of the lake. Except the entry area of Gumara river the absorption in all over the lake is high and approximately greater than 4m^{-1} (Figure 23). In general maximum IOPs were derived at this time.

7.4. Shortly after the end of rainy season (29 November 2013)

The suspended sediment was spread all over the lake and the resulting water leaving reflectance more or less equal throughout the lake. Both the absorption and scattering of the responsible constituents followed the same pattern of increase and decrease across the lake. The relative higher values of both IOPs (absorption and scattering) were derived from the northern part of the lake. During this period the measurement that will be taken from some parts of the lake approximately represent the other parts.

As studied by Wondie et al. (2007) and Vijverberg et al. (2009) and observed by this study, due to a low water transparency resulting from the high silt load of inflowing rivers during the rainy season and daily re-suspension of the sediment which affects the light propagation in to the water column; the lake has been characterized by low nutrient concentration and production rate. In general, the most important water quality constituent contributes to the IOPs of the lake is SPM.

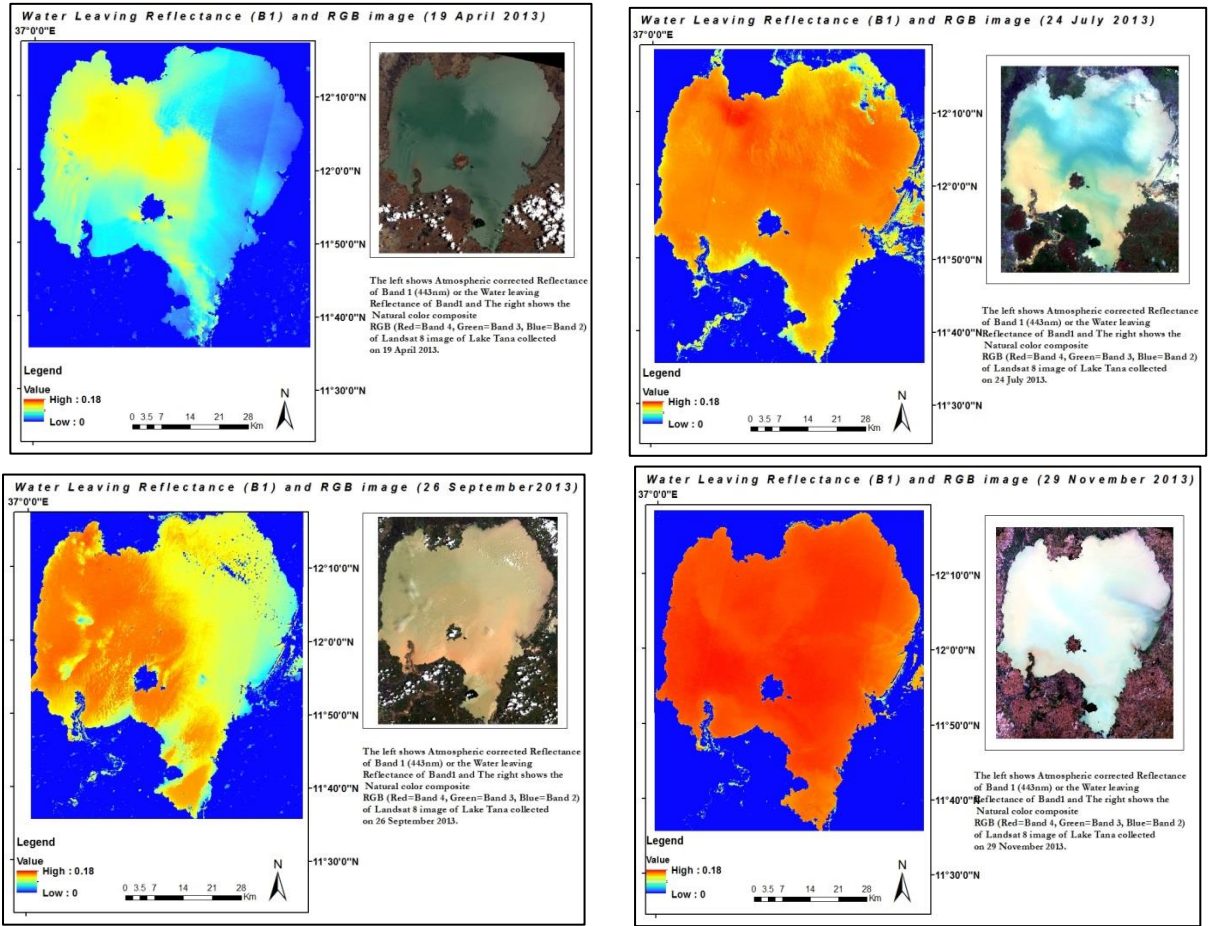


Figure 20 The Water Leaving Reflectance at Band 1(atmospheric corrected) and Natural Colour Composite of Lake Tana (19 April, 24 July, 26 September, and 29 November 2013)

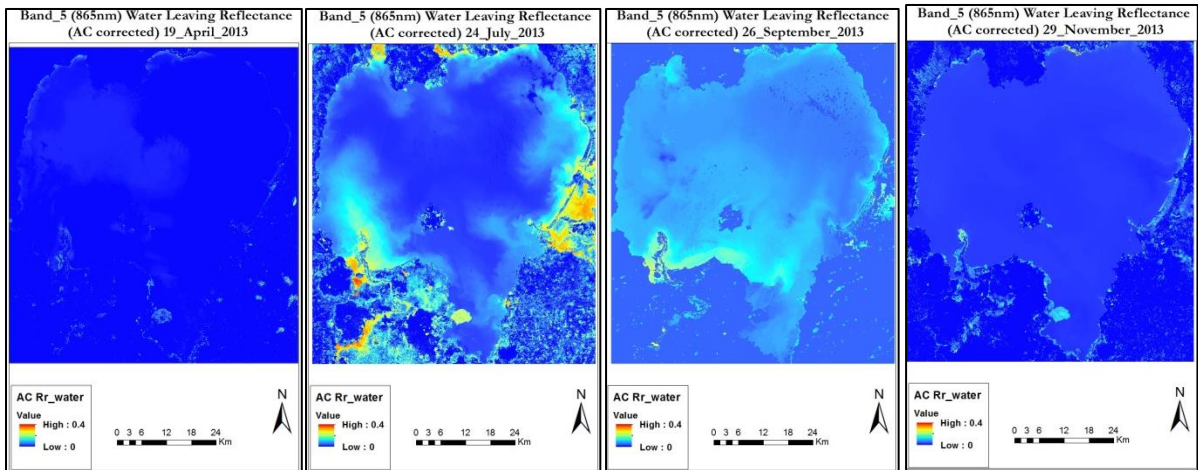


Figure 21 The Water Leaving Reflectance (Atmospheric corrected) at Band 5 (19 April, 24 July, 26 September, and 29 November 2013 from left to right)

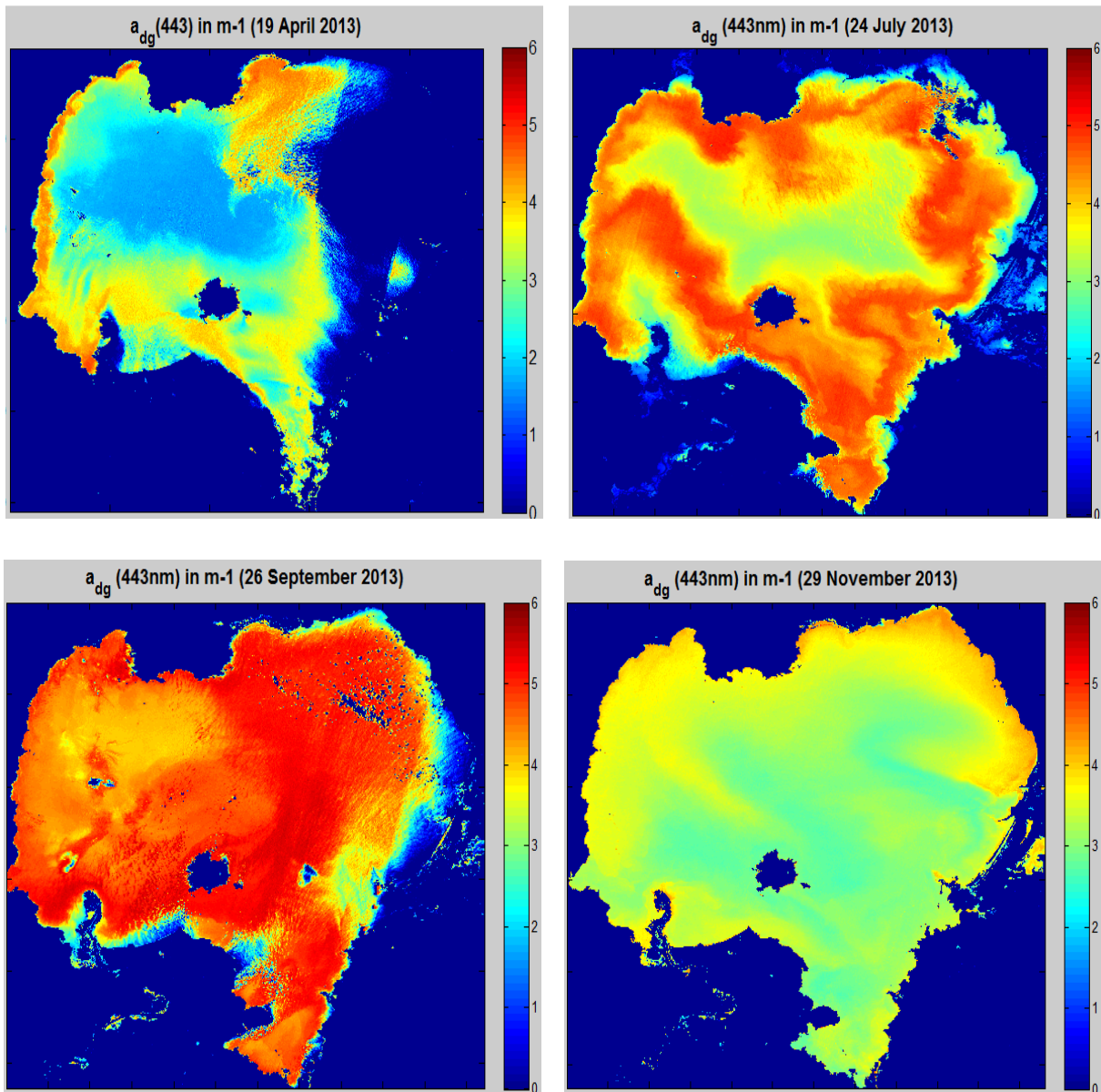


Figure 22 the absorption of detritus and gelbstoff at 443nm for the images of dry period, peak rainy season, end of rainy season, and shortly after the end of rainy season from left to right.

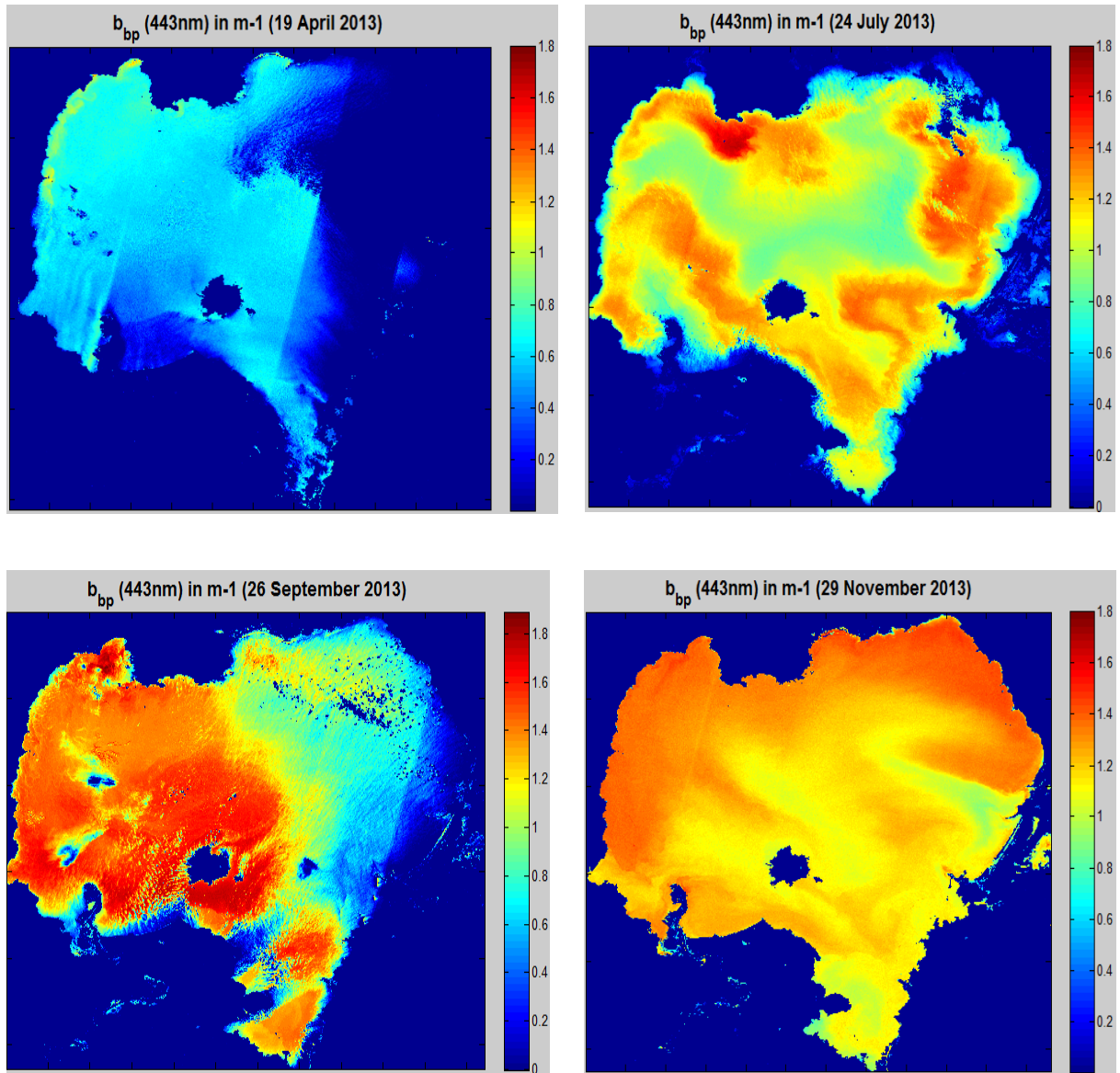


Figure 23 the backscattering coefficient of suspended particulate matter of Lake Tana for four different periods. Dry period, peak rainy season, end of rainy season and shortly after the end of rainy season from left to right.

8. CONCLUSION AND RECOMMENDATION

8.1. Conclusion

This study aimed at retrieving of water quality variables by satellite remote sensing for a data scarce Lake Tana region. The wavelength range of TriOS Ramses data to work accompany with OLI bands of Landsat-8 and the central wavelengths of the first five Landsat-8's OLI bands have been investigated as listed in Table 11.

Table 11 The wavelength range of TriOS Ramses data to work with Landsat-8's OLI bands

Landsat-8 bands	Wavelength range	Central wavelength
Band-1 (Deep Blue)	436-450	443
Band-2 (Blue)	454-511	482.5
Band-3 (Green)	535-588	566.5
Band-4 (Red)	637-672	654.5
Band-5 (NIR)	852 - 877	864.5

The Hydrosat originally developed to derive the water quality variables from Landsat Enhanced Thematic Mapper-plus (Landsat-ETM) which is from Landsat-7 has been modified to retrieve the water quality indicators from Landsat-8. The original Hydrosat considered the reflectance from four bands of Landsat-ETM, three in visible and one in near infrared (Salama et al., 2012b). While in addition to shortwave infrared (band-6) and cirrus (band-9) of OLI bands which have been used in atmospheric correction process, the modified Hydrosat considers five Landsat-8 OLI bands for the water quality retrieval, four in visible and one in NIR. Therefore, the recently launched LDCM's Landsat-8 with high spatial resolution has been found reliable to derive the water quality indicators of the lakes and its spectral setup has improved the accuracy of IOPs retrieval. Newly added bands of Landsat-8 (band-1 and band-9) have been found useful in the water quality variables retrieval process. Band-1 can be used to derive most common water quality indicators and band-9 can be used for the first haze correction.

The verification made on Hydrosat atmospheric correction method reduced 52% and 45% relative root mean square error in deep blue and blue region, respectively (Table 9). Whereas the verified and original Hydrosat returned approximately equal values for the bands from Green to NIR.

The derived IOPs (absorption of detritus and gelbstoff, and backscattering coefficients of SPM) and measured SPM concentration showed a strong linear relationship with R-squared value of greater than 0.7. However during rainy season the relation between absorption of detritus and gelbstoff with measured CDOM concentration is weak and unrealistic; and the phytoplankton effect can be neglected. Therefore the most important optically significant constituent of the Lake Tana is SPM and caused by a high load of suspended sediment from the tributaries and surrounding agricultural areas. The estimated specific backscattering coefficient (SIOP) of SPM ($b_{b,spm}^*$ (443)) of Lake Tana is $0.0091\text{m}^2/\text{g}$. The estimated value of SIOP of SPM at 443nm has been considered as spatially constant and resulted in reliable retrieval of SPM with R-squared value greater than 0.7.

The following conclusions have been drawn on spatial and temporal water quality status of Lake Tana.

- During the dry season the most likely absorbing constituents are CDOM and the water molecule. Except in the northwest central part (absorption between 1 and 3m^{-1}) the absorption is high

(between 3 and 5m⁻¹) in the other parts of the lake. In most parts of the lake the backscattering of SPM is low (less than 0.7m⁻¹) in this season, and relatively higher SPM was shown (backscattering between 0.7 and 1.2m⁻¹) in the northwest part of the lake.

- During the peak rainy season both absorption and backscattering were governed by SPM and followed the same pattern throughout the lake. The sediment loads from the tributaries are the important factor to increase IOPs in the river outlet and along the sides of the lake. In almost all parts of the lake the range of absorption is between 3 to 6m⁻¹, and backscattering is between 0.8 to 1.7m⁻¹.
- At the end of rainy season the SPM concentration is low in the east and northeast part of the lake and high in the west part of the lake. Except a small area around the outlet of Gumara river, in almost all other parts of the lake the absorption is high (between 4 and 6m⁻¹). The absorbing constituents in the east part of the lake are higher than the west part. The most dominant absorber in the west is detritus and in the northwest the most likely absorbers are both detritus and gelbstoff.
- Shortly after the end of rainy season the IOPs (both absorption and backscattering) were maximum in the northern part of the lake. However the relative overall distributions of IOPs are approximately equal. At this period the SPM spread all over the lake and affected both absorption and backscattering.

Finally on the image of Lake Tana acquired on 19 of April 2013 there is uncertainty on its east part (Figure 20). The uncertainty may be from the sensor noise. For water body with high absorption characteristics the remote sensing reflectance value at 443nm relatively small. Therefore, the adopted model on this area might not perform properly because of low signal-to-noise-ratios.

8.2. Recommendation

Covering the entire lake and getting cloud free images for the matchup during the short field measurement period were the biggest challenge of the study. From the two available images of Landsat-8 of the field measurement period one image was cloudy and wasn't useful for the study. It's obvious that the field measurement didn't cover the entire lake area. To investigate all optically significant water quality constituents and to get more reliable IOPs, the following recommendations have been made:

- More intensive and frequent water quality field measurements with simultaneous matchup images collection are recommended in order to get more reliable information on IOPs.
- Follow-up studies should use the newly reprocessed calibration parameters for Landsat-8.
- Further investigation on the source of uncertainty occurred on the acquired image (19 of April 2013) is suggested.

LIST OF REFERENCES

- Abreham Kibret, A. (2009). *Open water evaporation estimation using ground measurements and satellite remote sensing : a case study of lake Tana, Ethiopia*. ITC, Enschede. Retrieved from http://www.itc.nl/library/papers_2009/msc/wrem/kibret.pdf
- Alemayehu, T., McCartney, M., & Kebede, S. (2009). Simulation of water resource development and environmental flows in the Lake Tana Sub basin. *Improved Water and Land Management in the Ethiopian Highlands: Its Impact on Downstream Stakeholders Dependent on the Blue Nile*, 23.
- Austin, R. W., & Petzold, T. J. (1986). Spectral Dependence Of The Diffuse Attenuation Coefficient Of Light In Ocean Waters. *Optical Engineering*, 25(3), 253471-253471-. doi: 10.1117/12.7973845
- Ayana, E. K. (2013). *Remote Sensing Tools for Land and Water Management in Data Scarce Blue Nile Basin*. Cornell University.
- Babin, M., Stramski, D., Ferrari, G. M., Claustre, H., Bricaud, A., Obolensky, G., & Hoepffner, N. (2003). Variations in the light absorption coefficients of phytoplankton, nonalgal particles, and dissolved organic matter in coastal waters around Europe. *Journal of Geophysical Research: Oceans*, 108(C7), 3211. doi: 10.1029/2001JC000882
- Briucaud, A., Morel, A., & Prieur, L. (1981). Absorption by dissolved organic matter of the sea (yellow substance) in the UV and visible domains. *Limnology and Oceanography*, 26(1), 43-53. doi: 10.4319/lo.1981.26.1.0043
- Ciotti, A. M., Lewis, M. R., & Cullen, J. J. (2002). Assessment of the relationships between dominant cell size in natural phytoplankton communities and the spectral shape of the absorption coefficient. *Limnology and Oceanography*, 47(2), 404-417.
- Dekker, A. G., Vos, R. J., & Peters, S. W. M. (2001). Comparison of remote sensing data, model results and in situ data for total suspended matter (TSM) in the southern Frisian lakes. *Science of The Total Environment*, 268(1-3), 197-214. doi: [http://dx.doi.org/10.1016/S0048-9697\(00\)00679-3](http://dx.doi.org/10.1016/S0048-9697(00)00679-3)
- Fargion, G. S., & Mueller, J. L. (2000). *Ocean optics protocols for satellite ocean color sensor validation, Revision 2*: National Aeronautics and Space Administration, Goddard Space Flight Center.
- Garver, S. A., & Siegel, D. A. (1997). Inherent optical property inversion of ocean color spectra and its biogeochemical interpretation: 1. Time series from the Sargasso Sea. *Journal of Geophysical Research: Oceans*, 102(C8), 18607-18625. doi: 10.1029/96JC03243
- Gebremariame, Z. H. (2009). *Assessment of climate change impact on the net basin supply of lake Tana water balance*. ITC, Enschede. Retrieved from http://www.itc.nl/library/papers_2009/msc/wrem/zeryehun.pdf
- GEOSS. (2007). GEO Inland and nearshore coastal water quality remote sensing. In M. Bauer, A. Dekker, P. DiGiacomo, S. Greb, A. Gitelson, A. Herlevi & T. Kutser (Eds.): GEOSS group on earth observation.
- Ghezehegn, S. G. (2011). *Deriving inherent optical properties and associated inversion : uncertainties in the Naivasha lake*. (MSc. Thesis), University of Twente Faculty of Geo-Information and Earth Observation (ITC), Enschede.
- Giardino, C., Bresciani, M., Villa, P., & Martinelli, A. (2010). Application of Remote Sensing in Water Resource Management: The Case Study of Lake Trasimeno, Italy. *Water Resources Management*, 24(14), 3885-3899. doi: 10.1007/s11269-010-9639-3
- Goody, R. (1964). Atmospheric radiation: Clarendon Press (Oxford).
- Gordon, H. R. (1997). Atmospheric correction of ocean color imagery in the Earth Observing System era. *Journal of Geophysical Research-Atmospheres*, 102(D14), 17081-17106. doi: 10.1029/96jd02443
- Gordon, H. R., Brown, J. W., & Evans, R. H. (1988a). Exact Rayleigh scattering calculations for use with the Nimbus-7 Coastal Zone Color Scanner. *Appl. Opt.*, 27(5), 862-871.
- Gordon, H. R., Brown, O. B., Evans, R. H., Brown, J. W., Smith, R. C., Baker, K. S., & Clark, D. K. (1988b). A semianalytic radiance model of ocean color. *Journal of Geophysical Research: Atmospheres*, 93(D9), 10909-10924. doi: 10.1029/JD093iD09p10909
- Gordon, H. R., Brown, O. B., & Jacobs, M. M. (1975). Computed relationships between the inherent and apparent optical properties of a flat homogeneous ocean. *Applied Optics*, 14(2), 417-427.

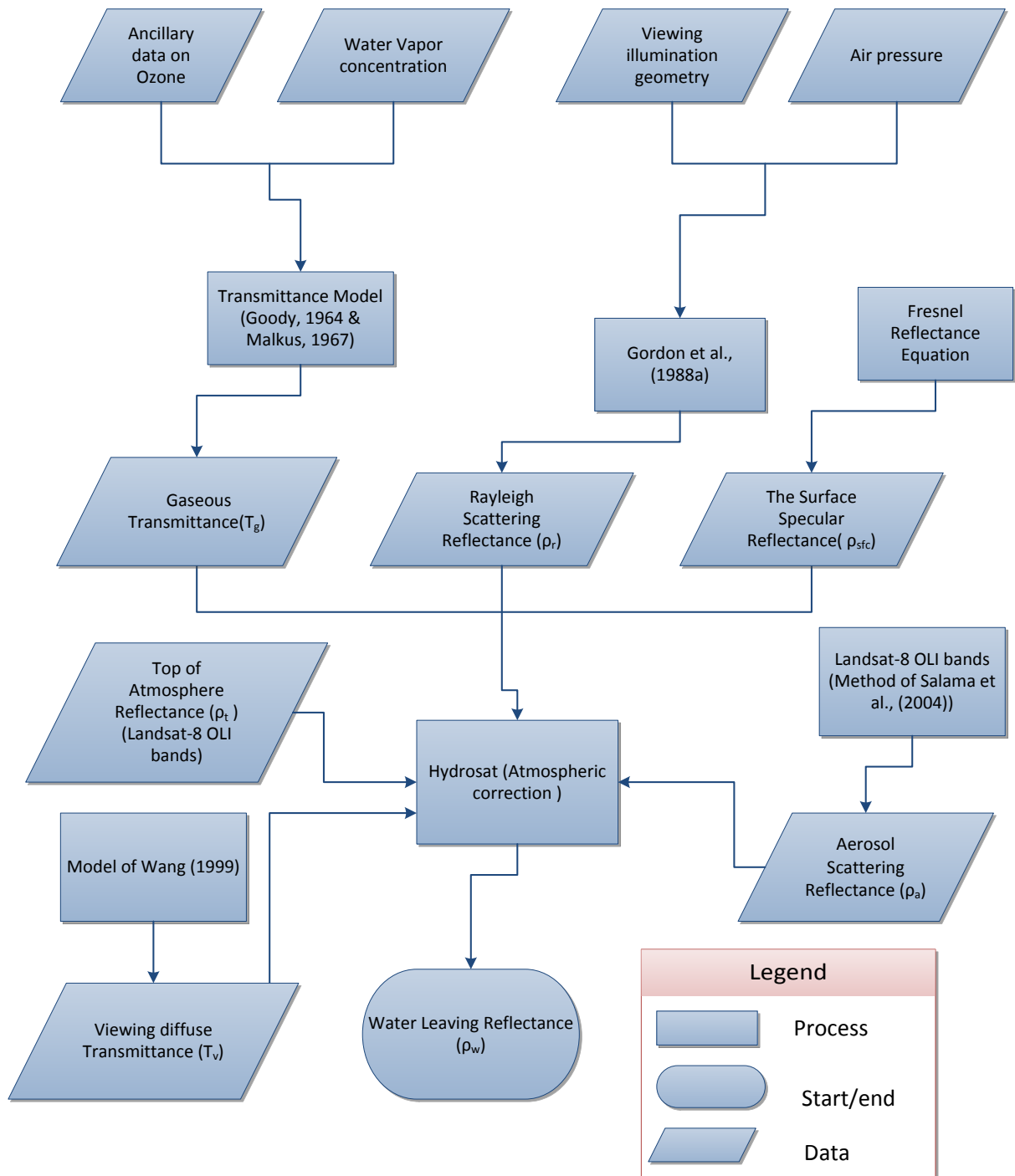
- Gordon, H. R., Clark, D. K., Brown, J. W., Brown, O. B., Evans, R. H., & Broenkow, W. W. (1983). Phytoplankton pigment concentrations in the Middle Atlantic Bight: Comparison of ship determinations and CZCS estimates. *Applied Optics*, 22(1), 20-36.
- Haltrin, V. I., & Kattawar, G. W. (1991). Effects of Raman scattering and fluorescence on apparent optical properties of seawater. *Report, Department of Physics, Texas A&M University, College Station, TX.*
- Hoge, F. E., & Lyon, P. E. (1996). Satellite retrieval of inherent optical properties by linear matrix inversion of oceanic radiance models: an analysis of model and radiance measurement errors. *Journal of Geophysical Research*, 101(C7), 16631-16616,16648.
- Hooker, S. B., & Maritorena, S. (2000). An evaluation of oceanographic radiometers and deployment methodologies. *Journal of Atmospheric & Oceanic Technology*, 17(6).
- IOCCG. (2006). Remote sensing of inherent optical properties: fundamentals, tests of algorithms, and applications. In Z. Lee (Ed.): Reports of the International Ocean-Colour Coordinating Group No. 5, IOCCG, Dartmouth, Canada.
- Kaba Ayana, E. (2007). *Validation of radar altimetry lake level data and it's application in water resource management.* ITC, Enschede.
- Kebede, S., Travi, Y., Alemayehu, T., & Marc, V. (2006). Water balance of Lake Tana and its sensitivity to fluctuations in rainfall, Blue Nile basin, Ethiopia. *Journal of Hydrology*, 316(1), 233-247.
- Kirk, J. T. O. (1994). *Light and photosynthesis in aquatic ecosystems:* Cambridge university press.
- Lee, Z.-P., Darecki, M., Carder, K. L., Davis, C. O., Stramski, D., & Rhea, W. J. (2005). Diffuse attenuation coefficient of downwelling irradiance: An evaluation of remote sensing methods. *Journal of Geophysical Research: Oceans*, 110(C2), C02017. doi: 10.1029/2004JC002573
- Lee, Z., Carder, K. L., Mobley, C. D., Steward, R. G., & Patch, J. S. (1998). Hyperspectral remote sensing for shallow waters. I. A semianalytical model. *Applied Optics*, 37(27), 6329-6338.
- Lee, Z., Carder, K. L., Mobley, C. D., Steward, R. G., & Patch, J. S. (1999). Hyperspectral Remote Sensing for Shallow Waters. 2. Deriving Bottom Depths and Water Properties by Optimization. *Appl. Opt.*, 38(18), 3831-3843.
- Li, L., Li, L., Song, K., Li, Y., Tedesco, L. P., Shi, K., & Li, Z. (2013). An inversion model for deriving inherent optical properties of inland waters: Establishment, validation and application. *Remote Sensing of Environment*, 135(0), 150-166. doi: <http://dx.doi.org/10.1016/j.rse.2013.03.031>
- Lindell, T., Pierson, D., & Premazzi, G. (1999). Manual for monitoring European lakes using remote sensing techniques.
- Malkmus, W. (1967). Random Lorentz Band Model with Exponential-Tailed S-1 Line-Intensity Distribution Function. *J. Opt. Soc. Am.*, 57(3), 323-329.
- Maritorena, S., Siegel, D., & Peterson, A. (2002). Optimization of a semianalytical ocean color model for global-scale applications. *Applied Optics*, 41(15), 2705-2714.
- Matsuoka, A., Hill, V., Huot, Y., Babin, M., & Bricaud, A. (2011). Seasonal variability in the light absorption properties of western Arctic waters: Parameterization of the individual components of absorption for ocean color applications. *Journal of Geophysical Research: Oceans*, 116(C2), C02007. doi: 10.1029/2009JC005594
- Minale, A., & Rao, K. (2011). Hydrological dynamics and human impact on ecosystems of Lake Tana, northwestern Ethiopia. *Ethiopian Journal of Environmental Studies and Management*, 4(1).
- Mobley, C. D. (1999). Estimation of the Remote-Sensing Reflectance from Above-Surface Measurements. *Applied Optics*, 38(36), 7442-7455. doi: 10.1364/AO.38.007442
- Mobley, C. D. (2004). *Light and water: Radiative transfer in natural waters* (Vol. 592): Academic press San Diego.
- Morel, A., & Prieur, L. (1977). Analysis of variations in ocean color. *Limnol. Oceanogr.*, 22(4), 709-722.
- Nigatu, Z. M. (2013). *Hydrological impacts of climate change on Lake Tana's water balance.* University of Twente Faculty of Geo-Information and Earth Observation (ITC), Enschede. Retrieved from http://www.itc.nl/library/papers_2013/msc/wrem/mulushewanigatu.pdf
- Palstra, A. P., de Graaf, M., & Sibbing, F. A. (2004). Riverine spawning and reproductive segregation in a lacustrine cyprinid species flock, facilitated by homing? *Animal Biology*, 54(4), 393-415.
- Pope, R. M., & Fry, E. S. (1997). Absorption spectrum (380-700 nm) of pure water. II. Integrating cavity measurements. *Appl. Opt.*, 36(33), 8710-8723.

- Preisendorfer, R. W. (1976). *Hydrologic Optics: Introduction* (Vol. 1): US Dept. of Commerce, National Oceanic and Atmospheric Administration, Environmental Research Laboratories, Pacific Marine Environmental Laboratory.
- Rientjes, T., Haile, A. T., & Fenta, A. A. (2013). Diurnal rainfall variability over the Upper Blue Nile Basin: A remote sensing based approach. *International Journal of Applied Earth Observation and Geoinformation*, 21(0), 311-325. doi: <http://dx.doi.org/10.1016/j.jag.2012.07.009>
- Rientjes, T., Perera, B., Haile, A., Reggiani, P., & Muthuwatta, L. (2011). Regionalisation for lake level simulation-the case of Lake Tana in the Upper Blue Nile, Ethiopia. *Hydrology & Earth System Sciences*, 15(4).
- Ritchie, J. C., Cooper, C. M., & Yongqing, J. (1987). Using landsat multispectral scanner data to estimate suspended sediments in Moon Lake, Mississippi. *Remote Sensing of Environment*, 23(1), 65-81. doi: [http://dx.doi.org/10.1016/0034-4257\(87\)90071-X](http://dx.doi.org/10.1016/0034-4257(87)90071-X)
- Salama, M., Velde, R., Woerd, H., Kromkamp, J., Philippart, C., Joseph, A., O'Neill, P., Lang, R., Gish, T., & Werdell, P. (2012a). Technical Note: Calibration and validation of geophysical observation models. *Biogeosciences*, 9(6), 2195-2201.
- Salama, M. S., Dekker, A., Su, Z., Mannaerts, C. M., & Verhoef, W. (2009). Deriving inherent optical properties and associated inversion-uncertainties in the Dutch Lakes. *Hydrology and Earth System Sciences*, 13(7), 1113-1121.
- Salama, M. S., Monbaliu, J., & Coppin, P. (2004). Atmospheric correction of advanced very high resolution radiometer imagery. *International journal of remote sensing*, 25(7-8), 1349-1355.
- Salama, M. S., Radwan, M., & van der Velde, R. (2012b). A hydro-optical model for deriving water quality variables from satellite images (HydroSat): A case study of the Nile River demonstrating the future Sentinel-2 capabilities. *Physics and Chemistry of the Earth, Parts A/B/C*, 50-52(0), 224-232. doi: <http://dx.doi.org/10.1016/j.pce.2012.08.013>
- Salama, M. S., & Shen, F. (2010). Simultaneous atmospheric correction and quantification of suspended particulate matters from orbital and geostationary earth observation sensors. *Estuarine, Coastal and Shelf Science*, 86(3), 499-511. doi: <http://dx.doi.org/10.1016/j.ecss.2009.10.001>
- Salama, M. S., & Stein, A. (2009a). Error decomposition and estimation of inherent optical properties. *Applied Optics*, 48(26), 4947-4962.
- Salama, M. S., & Stein, A. (2009b). Error decomposition and estimation of inherent optical properties. *Appl. Opt.*, 48(26), 4947-4962.
- Sasaki, H., Miyamura, T., Saitoh, S.-i., & Ishizaka, J. (2005). Seasonal variation of absorption by particles and colored dissolved organic matter (CDOM) in Funka Bay, southwestern Hokkaido, Japan. *Estuarine, Coastal and Shelf Science*, 64(2-3), 447-458. doi: <http://dx.doi.org/10.1016/j.ecss.2005.03.008>
- Setegn, S. G. (2010). *Modelling Hydrological and Hydrodynamic Processes in Lake Tana Basin, Ethiopia*. KTH.
- Setegn, S. G., Rayner, D., Melesse, A. M., Dargahi, B., & Srinivasan, R. (2011). Impact of climate change on the hydroclimatology of Lake Tana Basin, Ethiopia. *Water Resources Research*, 47(4), W04511. doi: 10.1029/2010wr009248
- Setegn, S. G., Srinivasan, R., Dargahi, B., & Melesse, A. M. (2009). Spatial delineation of soil erosion vulnerability in the Lake Tana Basin, Ethiopia. *Hydrological Processes*, 23(26), 3738-3750. doi: 10.1002/hyp.7476
- Smith, R. C., & Baker, K. S. (1981). Optical properties of the clearest natural waters(200-800 nm). *Applied Optics*, 20(2), 177-184.
- Stedmon, C. A., Markager, S., & Kaas, H. (2000). Optical Properties and Signatures of Chromophoric Dissolved Organic Matter (CDOM) in Danish Coastal Waters. *Estuarine, Coastal and Shelf Science*, 51(2), 267-278. doi: <http://dx.doi.org/10.1006/ecss.2000.0645>
- Upul Janaka Perera, B. (2009). *Ungauged catchment hydrology : the case of Lake Tana basin*. ITC, Enschede. Retrieved from http://www.itc.nl/library/papers_2009/msc/wrem/perera.pdf
- Vijverberg, J., Sibbing, F., & Dejen, E. (2009). Lake Tana: Source of the Blue Nile. In H. Dumont (Ed.), *The Nile* (Vol. 89, pp. 163-192): Springer Netherlands.
- Wale, A. (2008). *Hydrological balance of Lake Tana upper Blue Nile basin, Ethiopia*. (MSc. Thesis), ITC, Enschede.
- Wale, A., Rientjes, T. H. M., Dost, R. J. J., & Gieske, A. S. M. (2008). Hydrological balance of Lake Tana, upper Blue Nile basin, Ethiopia. In: *Proceedings of the workshop on hydrology and ecology of the Nile river*

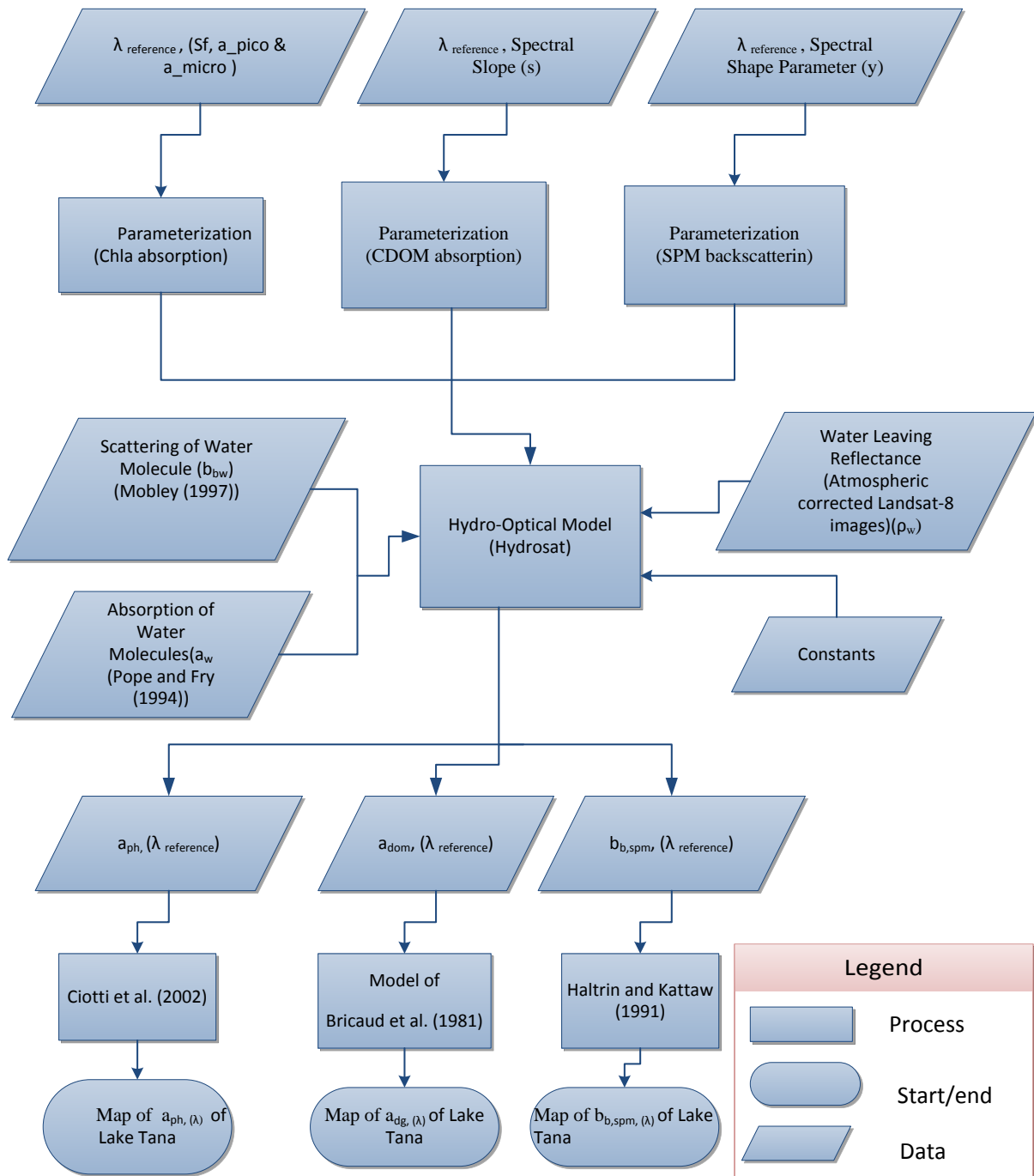
basin under extreme conditions : Addis Ababa, Ethiopia, June 16-19, 2008 / editor W. Abten, A.M. Melesse. - Miami : Florida International University, 2008. ISBN 978-1-4276-3150-3. pp. 159-180.

- Wang, G., Cao, W., Yang, D., & Xu, D. (2008). Variation in downwelling diffuse attenuation coefficient in the northern South China Sea. *Chinese Journal of Oceanology and Limnology*, 26(3), 323-333. doi: 10.1007/s00343-008-0323-x
- Wang, M. (1999). Atmospheric correction of ocean color sensors: computing atmospheric diffuse transmittance. *Applied Optics*, 38(3), 451-455.
- Wang, P., Boss, E. S., & Roesler, C. (2005). Uncertainties of inherent optical properties obtained from semianalytical inversions of ocean color. *Applied Optics*, 44(19), 4074-4085. doi: 10.1364/ao.44.004074
- Wondie, A., Mengistu, S., Vijverberg, J., & Dejen, E. (2007). Seasonal variation in primary production of a large high altitude tropical lake (Lake Tana, Ethiopia): effects of nutrient availability and water transparency. *Aquatic Ecology*, 41(2), 195-207.
- Zaneveld, J. R., Barnard, A., & Boss, E. (2005). Theoretical derivation of the depth average of remotely sensed optical parameters. *Optics express*, 13(22), 9052-9061.
- Zhang, Y., Zhang, B., Wang, X., Li, J., Feng, S., Zhao, Q., Liu, M., & Qin, B. (2007). A study of absorption characteristics of chromophoric dissolved organic matter and particles in Lake Taihu, China. *Hydrobiologia*, 592(1), 105-120. doi: 10.1007/s10750-007-0724-4

APPENDIX 1. ATMOSPHERIC CORRECTION METHOD (HYDROSAT)



APPENDIX 2. WATER QUALITY RETRIEVAL (HYDROSAT METHOD)



APPENDIX 3. RELATIVE SPECTRAL RESPONSE (RSR) OF LANDSAT-8

W _{ave} - length (CA)	RSR	W _{ave} - length (Blue)	RSR	W _{ave} - Length (Green)	RSR	W _{ave} - length (Red)	RSR	W _{ave} - length (NIR)	RSR	W _{ave} - length	RSR
427	0.000073	436	0.00001	512	-4.6E-05	625	-0.00034	829	-3.4E-05	1340	-3E-06
428	0.000609	437	0.000061	513	0.000016	626	0.00027	830	0.000011	1341	0.000086
429	0.001628	438	0.000117	514	0.00011	627	0.000895	831	0.00005	1342	0.000194
430	0.003421	439	0.000241	515	0.000247	628	0.00185	832	0.0001	1343	0.000321
431	0.008019	440	0.000349	516	0.000362	629	0.003648	833	0.000239	1344	0.000469
432	0.024767	441	0.000455	517	0.000648	630	0.007197	834	0.000314	1345	0.000647
433	0.085688	442	0.000756	518	0.000935	631	0.014515	835	0.000495	1346	0.000856
434	0.254149	443	0.001197	519	0.001332	632	0.030432	836	0.000719	1347	0.001119
435	0.517821	444	0.00207	520	0.001816	633	0.066861	837	0.000986	1348	0.001429
436	0.765117	445	0.003712	521	0.002515	634	0.148518	838	0.001445	1349	0.001828
437	0.908749	446	0.006869	522	0.003446	635	0.299778	839	0.002107	1350	0.002318
438	0.958204	447	0.013212	523	0.00488	636	0.526812	840	0.00316	1351	0.00303
439	0.977393	448	0.02717	524	0.007024	637	0.764443	841	0.004744	1352	0.004011
440	0.98379	449	0.058606	525	0.010441	638	0.905473	842	0.007059	1353	0.005398
441	0.989052	450	0.130876	526	0.016247	639	0.947949	843	0.0109	1354	0.007194
442	0.986713	451	0.27137	527	0.025513	640	0.950823	844	0.017346	1355	0.011124
443	0.993683	452	0.493542	528	0.041451	641	0.947418	845	0.028332	1356	0.016985
444	0.993137	453	0.723971	529	0.070551	642	0.951831	846	0.048191	1357	0.026321
445	1	454	0.85751	530	0.123444	643	0.962705	847	0.084363	1358	0.042756
446	0.996969	455	0.894222	531	0.21168	644	0.975075	848	0.145365	1359	0.06922

DERIVING WATER QUALITY INDICATORS OF LAKE TANA, ETHIOPIA, FROM LANDSAT-8

447	0.98278	456	0.903034	532	0.353885	645	0.984173	849	0.249733	1360	0.115351
448	0.972692	457	0.910928	533	0.545856	646	0.983613	850	0.403526	1361	0.182833
449	0.905808	458	0.90988	534	0.741205	647	0.983434	851	0.582623	1362	0.316333
450	0.745606	459	0.899475	535	0.865225	648	0.982911	852	0.745037	1363	0.45703
451	0.471329	460	0.897977	536	0.927396	649	0.973636	853	0.890315	1364	0.596852
452	0.226412	461	0.889667	537	0.954627	650	0.959441	854	0.960215	1365	0.772118
453	0.09286	462	0.883542	538	0.954163	651	0.955641	855	0.986833	1366	0.862394
454	0.036603	463	0.877453	539	0.959215	652	0.955548	856	0.973133	1367	0.871575
455	0.014537	464	0.881011	540	0.961328	653	0.953337	857	0.980606	1368	0.930308
456	0.005829	465	0.874721	541	0.964902	654	0.956628	858	0.99612	1369	0.962664
457	0.002414	466	0.879688	542	0.969873	655	0.981688	859	1	1370	0.931247
458	0.000984	467	0.886569	543	0.952489	656	1	860	0.989777	1371	0.938676
459	0.000255	468	0.891913	544	0.961397	657	0.992388	861	0.980733	1372	0.983748
		469	0.88768	545	0.97827	658	0.984615	862	0.975935	1373	0.999626
		470	0.861157	546	0.977533	659	0.981568	863	0.972043	1374	0.986968
		471	0.848533	547	0.977001	660	0.97696	864	0.957357	1375	1
		472	0.840828	548	0.980884	661	0.97298	865	0.951209	1376	0.983239
		473	0.828339	549	0.990784	662	0.98108	866	0.947044	1377	0.990577
		474	0.844202	550	1	663	0.996804	867	0.953162	1378	0.963584
		475	0.865864	551	0.992264	664	0.992142	868	0.951499	1379	0.964054
		476	0.868497	552	0.982642	665	0.980678	869	0.94845	1380	0.871343
		477	0.890253	553	0.983832	666	0.964002	870	0.940094	1381	0.872689
		478	0.912538	554	0.977765	667	0.962154	871	0.950632	1382	0.703198
		479	0.910385	555	0.965081	668	0.970778	872	0.956079	1383	0.606578
		480	0.918822	556	0.957314	669	0.96718	873	0.96646	1384	0.452434
		481	0.931726	557	0.946245	670	0.966928	874	0.969821	1385	0.29792
		482	0.931813	558	0.947871	671	0.949928	875	0.93661	1386	0.190978

